

# $V_{cs}$ from $D_s \rightarrow \phi l \nu$ semileptonic decay and full lattice QCD

G. C. Donald,<sup>1,\*</sup> C. T. H. Davies,<sup>1,†</sup> J. Koponen,<sup>1</sup> and G. P. Lepage<sup>2</sup>  
(HPQCD collaboration),<sup>‡</sup>

<sup>1</sup>*SUPA, School of Physics and Astronomy, University of Glasgow, Glasgow, G12 8QQ, UK*  
<sup>2</sup>*Laboratory of Elementary-Particle Physics, Cornell University, Ithaca, New York 14853, USA*  
(Dated: February 28, 2024)

We determine the complete set of axial and vector form factors for the  $D_s \rightarrow \phi l \nu$  decay from full lattice QCD for the first time. The valence quarks are implemented using the Highly Improved Staggered Quark action and we normalise the appropriate axial and vector currents fully nonperturbatively. The  $q^2$  and angular distributions we obtain for the differential rate agree well with those from the BaBar experiment and, from the total branching fraction, we obtain  $V_{cs} = 1.017(63)$ , in good agreement with that from  $D \rightarrow K l \nu$  semileptonic decay. We also find the mass and decay constant of the  $\phi$  meson in good agreement with experiment, showing that its decay to  $K\bar{K}$  (which we do not include here) has at most a small effect. We include an Appendix on nonperturbative renormalisation of the complete set of staggered vector and axial vector bilinears needed for this calculation.

## I. INTRODUCTION.

The analysis of weak semileptonic decays in which one meson changes into another and emits a  $W$  boson provides a strong test of QCD. The test is complementary to that of comparing QCD predictions to experiment for the meson mass and leptonic decay constants, and in principle more stringent because, instead of just one number, the comparison involves the shape of a differential rate as a function of  $q^2$ , the square of the 4-momentum transfer from initial to final meson. The QCD information that appears in the differential rate, and the functions of  $q^2$  that are calculated in lattice QCD, are known as form factors. Lattice QCD calculations have largely focussed on pseudoscalar to pseudoscalar decays where only one form factor contributes to the experimental rate. Accurate tests against experiment have been carried out for, for example,  $D \rightarrow K l \nu$  decay [1]. Here we study the pseudoscalar to vector decay,  $D_s \rightarrow \phi l \nu$ , in which 3 form factors contribute to the experimental results. This allows us to compare angular distributions as well as differential rates in  $q^2$ , providing a more complete test of how QCD interactions that bind a quark inside a meson affect the quark weak decay process. This is the first time this calculation has been done in full lattice QCD including the effect of sea quarks.

The fundamental quark weak decay in  $D_s \rightarrow \phi l \nu$  is a  $c \rightarrow s$  transition and so comparison with experiment allows us to determine  $V_{cs}$ . This is then a direct determination of this CKM element which is independent of other methods such as  $D \rightarrow K l \nu$  semileptonic decay or  $D_s$  leptonic annihilation. Although our result is currently not as accurate as these other methods, it nevertheless

contributes to improving our confidence in the determination of  $V_{cs}$  and the second row and column CKM unitarity tests in which it plays a key role.

The  $D_s \rightarrow \phi$  decay has initial and final mesons with no light valence quarks. This is useful for a lattice QCD calculation which includes light quarks with masses that are heavier than the physical values since it means that the extrapolation in the light quark mass to the physical point only affects sea quark contributions and so is relatively benign. The  $\phi$  meson is likely to be more sensitive to light quark masses than the  $D_s$  because it has a strong decay mode to  $K\bar{K}$ . The  $\phi$  is below threshold for this decay in a lattice QCD calculation with heavier-than-physical light quark masses; it is only just above threshold when the light quarks have their physical masses. We will treat the  $\phi$  as stable in our lattice QCD calculation. By comparing the  $\phi$  decay constant we calculate on the lattice to the experimental rate, we can estimate the systematic error on matrix elements that can arise from ignoring the strong decay.

The  $q^2$  range for  $D_s \rightarrow \phi$  decay is not large, running from  $q_{max}^2 = (M_{D_s} - M_\phi)^2 = 0.898 \text{ GeV}^2$  to  $q^2 = 0$ . We can easily cover the entire range in a lattice QCD calculation, needing only  $p_\phi = 0.719 \text{ GeV}$  in the  $D_s$  rest frame to reach  $q^2 = 0$ . Discretisation errors are then small in a good discretisation such as the Highly Improved Staggered Quark formalism [2] that we use here. Since the entire range in  $q^2$  is covered we can make a detailed comparison to experimental distributions as a function of  $q^2$  and we can integrate over  $q^2$  to extract  $V_{cs}$  from a comparison to experiment of the total branching fraction.

The paper is laid out as follows: Section II describes the theoretical background and then Section III gives a general description of the lattice calculation. Section IV gives the details of the results, first for the  $\phi$  meson and then for each of the form factors for  $D_s \rightarrow \phi$  in turn, describing how they were calculated. A comparison to BaBar's experimental results is then made for the form factors and for the differential distributions as a function of  $q^2$  and decay product angles and finally  $V_{cs}$  is deter-

\*Current address: School of Mathematics, Trinity College, Dublin 2, Ireland (donaldg@tcd.ie)

†christine.davies@glasgow.ac.uk

‡URL: <http://www.physics.gla.ac.uk/HPQCD>

mined from the total rate. In Section V we discuss the comparison between our form factors for  $D_s \rightarrow \phi$  with those extracted by CLEO from experiment for  $D \rightarrow K^*$ . Section VI gives our conclusions. In Appendix A we describe how to normalise all the form factors nonperturbatively and in Appendix B we give more details for the specific case of the 1-link axial current operator.

## II. THEORETICAL BACKGROUND

The matrix element of the hadronic weak  $V-A$  current between the pseudoscalar  $D_s$  and the vector  $\phi$  meson can be expressed in terms of form factors as [3]

$$\begin{aligned} & \langle \phi(p', \varepsilon) | V^\mu - A^\mu | D_s(p) \rangle \\ &= \frac{2i\varepsilon^{\mu\nu\alpha\beta}}{M_{D_s} + M_\phi} \varepsilon_\nu^* p'_\alpha p_\beta V(q^2) - (M_{D_s} + M_\phi) \varepsilon^{*\mu} A_1(q^2) \\ &+ \frac{\varepsilon^* \cdot q}{M_{D_s} + M_\phi} (p + p')^\mu A_2(q^2) + 2M_\phi \frac{\varepsilon^* \cdot q}{q^2} q^\mu A_3(q^2) \\ &- 2M_\phi \frac{\varepsilon^* \cdot q}{q^2} q^\mu A_0(q^2). \end{aligned} \quad (1)$$

Here  $\varepsilon$  is the polarization vector of the  $\phi$  meson and  $q^\mu = p^\mu - p'^\mu$ . The vector and axial vector currents are given in this case by  $\bar{c}\gamma^\mu s$  and  $\bar{c}\gamma^\mu\gamma^5 s$ .  $A_3$  is not an independent form factor since

$$A_3(q^2) = \frac{M_{D_s} + M_\phi}{2M_\phi} A_1(q^2) - \frac{M_{D_s} - M_\phi}{2M_\phi} A_2(q^2). \quad (2)$$

We also have the kinematic constraint that  $A_3(0) = A_0(0)$ . The form factors that appear with factors of  $q^\mu$  do not contribute significantly to the experimental rate when the  $W$  boson decays to  $e^+\nu_e$  or  $\mu^+\nu_\mu$ . The reason is that the expression in Eq. 1 is dotted into the leptonic current,  $L_\mu = \bar{\ell}\gamma_\mu(1 - \gamma_5)u_\nu$ , when forming the rate and  $q^\mu L_\mu \rightarrow 0$  as  $m_\ell \rightarrow 0$ . Thus the form factors that we need to calculate to compare to experiment are  $V(q^2)$ ,  $A_1(q^2)$  and  $A_2(q^2)$ .

In the lattice QCD calculation, to be described in section III, all of the form factors will appear in the matrix elements of the vector and axial vector currents that we calculate (as in Eq. 1), and we have to choose particular kinematic configurations to isolate each one. We will also use the matrix element of the pseudoscalar current,  $P = \bar{c}\gamma_5 s$ , to access some of the form factors. From the partially conserved axial current (PCAC),  $\partial_\mu A^\mu = (m_1 + m_2)P$ , which is exact for staggered quarks we have

$$\langle \phi(p', \varepsilon) | P | D_s(p) \rangle = \frac{2M_\phi \varepsilon^* \cdot q}{(m_c + m_s)} A_0(q^2). \quad (3)$$

As well as comparing the shape of the extracted form factors to experiment we can also compare the differential cross-section in bins of  $q^2$  or of the important angular variables for this decay. These angles are shown in Fig. 1 for results corresponding to the case where the  $\phi$  is seen

through its decay to  $K^+K^-$ .  $\theta_\ell$  is the angle between the momentum of the charged lepton and that of the  $W$  boson (= centre of momentum of the charged lepton and the neutrino) in the rest frame of the  $D_s$ .  $\theta_K$  is the angle between the momentum of one of the  $K$  mesons ( $K^+$  for  $D_s^+$  and  $K^-$  for  $D_s^-$ ) and the  $\phi$  (= centre of momentum for both  $K$  mesons).  $\chi$  is the angle between the two planes, one defined by the  $K$  meson pair and the other defined by the lepton pair.

The differential rate for the decay is then given in terms of helicity amplitudes as [3]

$$\begin{aligned} & \frac{d\Gamma(D_s \rightarrow \phi\ell\nu, \phi \rightarrow K^+K^-)}{dq^2 d\cos\theta_K d\cos\theta_\ell d\chi} = \\ & \frac{3}{8(4\pi)^4} G_F^2 |V_{cs}|^2 \frac{p_\phi q^2}{M_{D_s}^2} \mathcal{B}(\phi \rightarrow K^+K^-) \times \\ & \left\{ (1 + \cos\theta_\ell)^2 \sin^2\theta_K |H_+(q^2)|^2 \right. \\ & + (1 - \cos\theta_\ell)^2 \sin^2\theta_K |H_-(q^2)|^2 \\ & + 4 \sin^2\theta_\ell \cos^2\theta_K |H_0(q^2)|^2 \\ & + 4 \sin\theta_\ell (1 + \cos\theta_\ell) \sin\theta_K \cos\theta_K \cos\chi H_+(q^2) H_0(q^2) \\ & - 4 \sin\theta_\ell (1 - \cos\theta_\ell) \sin\theta_K \cos\theta_K \cos\chi H_-(q^2) H_0(q^2) \\ & \left. - 2 \sin^2\theta_\ell \sin^2\theta_K \cos 2\chi H_+(q^2) H_-(q^2) \right\}. \end{aligned} \quad (4)$$

$p_\phi$  is the momentum of the  $\phi$  in the  $D_s$  rest frame, in which we work.  $H_\pm, H_0$  correspond to contributions from different  $W$  helicities, and the  $W$  and  $\phi$  helicities are constrained to be the same because the parent meson has zero spin. Helicity information on the quark produced in the weak decay is lost in a pseudoscalar to pseudoscalar transition, because the final meson has no helicity. Here, in a pseudoscalar to vector transition it is not lost, and thus the distributions give more information about the  $V-A$  nature of the weak interaction. For a  $c \rightarrow s$  decay we expect a predominantly  $\lambda = -1/2$   $s$  quark to be produced, which can then form a helicity 0 or helicity -1 meson by combining with the spectator  $\bar{s}$  to form a  $\phi$ . Thus we expect  $H_-$  to dominate over  $H_+$ . The  $W$  in a  $c \rightarrow s$  decay is a  $W^+$  and therefore decays to  $\ell^+\nu$ . A fast-moving  $\ell^+$  will be predominantly  $\lambda = +1/2$  and therefore preferentially thrown backwards in the  $D_s$  rest frame to balance helicities. This explains the  $\cos\theta_\ell$  distributions for the term proportional to  $|H_-(q^2)|^2$  [3]. At low  $q^2$ , where the dominant configuration has the  $\ell^+$  and  $\nu$  in parallel, balancing the  $\phi$ ,  $H_0$  will dominate because the spins of  $\ell$  and  $\nu$  will cancel.

The helicity functions are related to the form factors as

$$H_\pm(q^2) = (M_{D_s} + M_\phi) A_1(q^2) \mp \frac{2M_{D_s} p_\phi}{M_{D_s} + M_\phi} V(q^2) \quad (5)$$

and

$$\begin{aligned} H_0(q^2) &= \frac{1}{2M_\phi \sqrt{q^2}} \times \\ & \left[ (M_{D_s}^2 - M_\phi^2 - q^2)(M_{D_s} + M_\phi) A_1(q^2) \right. \\ & \left. - 4 \frac{M_{D_s}^2 p_\phi^2}{M_{D_s} + M_\phi} A_2(q^2) \right]. \end{aligned} \quad (6)$$

The  $p_\phi q^2$  factor in the differential cross-section (Eq. 4) means that the contribution of  $H_0(q^2)$  does not diverge as  $q^2 \rightarrow 0$ . Note that  $A_1$  contributes to all helicities,  $A_2$  only to  $H_0$  and  $V$  only to  $H_\pm$ . At high  $q^2$  where  $p_\phi \rightarrow 0$ ,  $A_1$  dominates all of the helicities.

In the differential decay rate given in Eq. 4, the lepton mass is neglected. This is a good approximation for  $D_s \rightarrow \phi$  semileptonic decays where  $\ell = e, \mu$  and one which we make for our comparison with BaBar results [4], in which the final state lepton is an electron.

However, we can calculate in lattice QCD the contributions to the decay rate that are suppressed by factors of  $m_\ell^2$  and study their relative size. If we do not neglect the lepton mass, the decay rate also includes [5]

$$\begin{aligned} & \frac{3}{8(4\pi)^4} G_F^2 |V_{cs}|^2 \frac{p_\phi m_\ell^2}{M_{D_s}^2} \mathcal{B}(\phi \rightarrow K^+ K^-) \times \quad (7) \\ & \{ \sin^2 \theta_K \sin^2 \theta_\ell |H_+(q^2)|^2 \\ & + \sin^2 \theta_K \sin^2 \theta_\ell |H_-(q^2)|^2 \\ & + 4 \cos^2 \theta_K \cos^2 \theta_\ell |H_0(q^2)|^2 \\ & + 4 \cos^2 \theta_K |H_t(q^2)|^2 \\ & + \sin^2 \theta_K \sin^2 \theta_\ell \cos 2\chi H_+(q^2) H_-(q^2) \\ & + \sin 2\theta_K \sin 2\theta_\ell \cos 2\chi H_+(q^2) H_0(q^2) \\ & + \sin 2\theta_K \sin 2\theta_\ell \cos 2\chi H_-(q^2) H_0(q^2) \\ & + 2 \sin 2\theta_K \sin \theta_\ell \cos \chi H_+(q^2) H_t(q^2) \\ & + 2 \sin 2\theta_K \sin \theta_\ell \cos \chi H_-(q^2) H_t(q^2) \\ & + 8 \cos^2 \theta_K \cos \theta_\ell H_0(q^2) H_t(q^2) \}. \end{aligned}$$

All of the cross terms in Eq. 7 vanish on integration over  $\chi$ , apart from  $H_0(q^2)H_t(q^2)$ , which vanishes if we integrate over  $\cos \theta_\ell$ .

The helicity amplitude  $H_t(q^2)$  is given by

$$H_t(q^2) = \frac{2M_{D_s} p_\phi}{\sqrt{q^2}} A_0(q^2). \quad (8)$$

At  $q^2 = 0$ ,  $H_t(0) = H_0(0)$  because, for these kinematics,  $M_{D_s}^2 - M_\phi^2 = 2M_{D_s} p_\phi$  and we also have  $A_0(0) = A_3(0)$ . We can calculate  $A_0(q^2)$  using a pseudoscalar current (see Eq. 3), so it is straightforward to calculate  $H_t(q^2)$  in lattice QCD.

As  $H_t$  is proportional to  $1/\sqrt{q^2}$ , it is most important at low  $q^2$ . The effect of this helicity amplitude could be detected as a difference in the semileptonic decay rate with electrons or muons in the final state. It has been observed in the measurements of  $D \rightarrow K^* \ell \nu$  made by CLEO [6].

### III. LATTICE CALCULATION.

For the lattice QCD calculation we use the Highly Improved Staggered Quark action [2] for all the valence quarks. This action has very small discretisation errors,

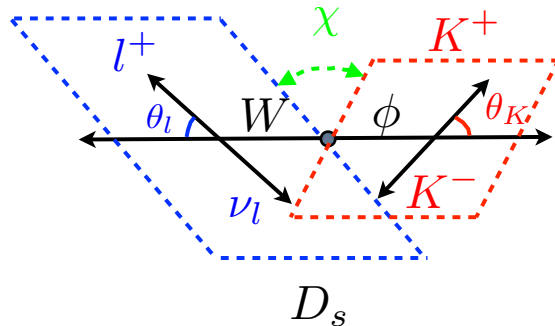


FIG. 1: Diagram to show the angles used for the differential rate for  $D_s \rightarrow \phi l \nu$ .  $l \nu$  are drawn in the virtual  $W^*$  rest frame and  $K^+ K^-$  in the  $\phi$  rest frame. The angles are defined in the  $D_s$  rest frame, however [3].

making it an excellent action for  $c$  [2, 7–9] as well as for the lighter  $s$  quarks we need here. We calculate HISQ propagators on gluon field configurations generated by the MILC collaboration that include  $u, d$  and  $s$  sea quarks using the asqtad formalism [10]. Table I gives the parameters of the ensembles of configurations we use, with two different lattice spacing values and two different  $u/d$  sea quark masses.

To tune the  $s$  and  $c$  quark masses to their correct physical values we use the pseudoscalar  $\eta_s$  and  $\eta_c$  meson masses [8]. The  $\eta_s$  is a fictitious  $s\bar{s}$  pseudoscalar that is not allowed to decay in lattice QCD. Although this meson does not occur in the real world its mass can be accurately determined in lattice QCD because it does not contain valence  $u/d$  quarks, and a ‘physical’ value for its mass can be determined in the continuum and chiral limits. We find  $M_{\eta_s} = 0.6858(40)$  GeV [11], and use this to tune the  $s$  quark mass [8]. In tuning the  $c$  quark mass here we must use the value of the  $\eta_c$  mass [8] in a world without electromagnetism or  $c$  quarks in the sea. We take this to be  $M_{\eta_c} = 2.985(3)$  GeV [12]. Discretisation errors from using the HISQ action are reduced for  $c$  quarks by modifying the coefficient of the ‘Naik’ term [13], which corrects for  $a^2$  errors in the covariant derivative, to include the tree-level correction which is a function of the bare quark mass,  $m_c a$  [8]. A measure of the smallness of the resulting discretisation errors comes from a study of the ‘speed of light’ for the  $\eta_c$  [9]. This differs from 1 by less than 3% on both the coarse and fine lattices.

The quark propagators are made from a ‘random wall’ source - a colour-vector of random numbers in  $U(1)$  on a source timeslice - to reduce the statistical noise. We use four evenly spaced time sources on each configuration, choosing the first time source randomly to reduce correlations between configurations.

The lattice spacing is determined for each ensemble using the calculation of static quark potential by MILC and the extraction of a parameter associated with that potential called  $r_1$  [10]. The value for this parameter in units of the lattice spacing,  $r_1/a$ , is given in Table I.

Set	$r_1/a$	$au_0m_l^{asq}$	$au_0m_s^{asq}$	$m_l/m_{s,phys}$	$L_s/a \times L_t/a$	$am_s^{HISQ}$	$am_c^{HISQ}$	$n_{cfg}$	$T$
1	2.647(3)	0.005	0.05	0.14	$24 \times 64$	0.0489	0.622	2088	12, 15, 18
2	2.618(3)	0.01	0.05	0.29	$20 \times 64$	0.0496	0.63	2259	12, 15, 18
3	3.699(3)	0.0062	0.031	0.24	$28 \times 96$	0.0337	0.413	1911	16, 19, 20, 23

TABLE I: Ensembles (sets) of MILC configurations used here. Sea (asqtad) quark masses  $m_\ell^{asq}$  ( $\ell = u/d$ ) and  $m_s^{asq}$  use the MILC convention where  $u_0$  is the plaquette tadpole parameter. The lattice spacing is given in units of  $r_1$  after ‘smoothing’ [10]. We use  $r_1 = 0.3133(23)$  fm [11]. Sets 1 and 2 are ‘coarse’ ( $a \approx 0.12$  fm) and set 3, ‘fine’ ( $a \approx 0.09$  fm). The lattice size is given by  $L_s^3 \times L_t$ . Column 5 gives the sea light quark mass in units of the physical strange mass, as determined in [8]. Columns 7 and 8 give the valence  $s$  and  $c$  HISQ quark masses, tuned to the physical values [8]. We use 4 time sources on each of the  $n_{cfg}$  configurations. The final column lists the  $T$  values used in the 3-pt correlators (see Fig. 2).

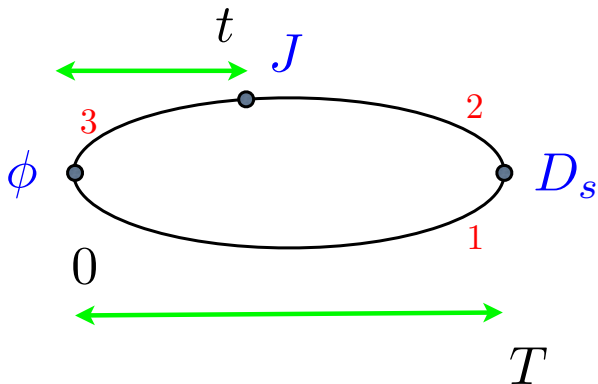


FIG. 2: A schematic diagram of the 3-point function for  $D_s \rightarrow \phi \nu$  decay. Different currents,  $J$ , are inserted at the vertex, as described in the text, to obtain specific form factors.

Using a physical value for  $r_1$ ,  $r_1 = 0.3133(23)$  fm [11], allows us to convert these numbers to a value for the lattice spacing,  $a$ , on each ensemble. This allows us in turn to convert all dimensionful quantities calculated on the lattice into GeV units.

The HISQ  $s$  and  $c$  quark propagators calculated on these gluon field configurations are combined to make meson correlators (2-point functions) for  $D_s$  and  $\phi$  and 3-point functions that allow us to calculate the  $D_s$  to  $\phi$  transition matrix element.

Correlators for mesons with specific spin-parity quantum numbers are made using staggered quarks (which have no spin degree of freedom) by including space-time-dependent phases of  $\pm 1$  at source and sink. This can be combined with a point-splitting of the source/sink operator. Because of fermion doubling there are 16 ‘tastes’ of every meson. We will use the spin-taste notation  $\gamma_n \otimes \gamma_s$  to denote a staggered bilinear with spin  $\gamma_n$  and taste  $\gamma_s$ . The masses of the different tastes differ by discretisation errors (at  $\mathcal{O}(a^2)$ ) and we are free to use whichever taste is the most convenient for each calculation. We will make use of that freedom here. However, because point-split source and sink operators typically give noisier results than local operators, we will restrict ourselves to at most a 1-link point-splitting.

We will use two different local operators to create/destroy  $D_s$  mesons. One is the local  $\gamma_5$  ‘Goldstone’

operator (i.e.  $\gamma_5 \otimes \gamma_5$ ) and the other is the local  $\gamma_t \gamma_5$  operator. The pattern of taste-splittings for pseudoscalar mesons is well mapped out and significantly reduced for HISQ quarks [2] over those in the asqtad formalism [14]. We expect splittings in the squared-mass of the different pseudoscalar tastes to be proportional to  $a^2$ . The lightest pseudoscalar is the Goldstone meson and the next lightest is that of the local  $\gamma_t \gamma_5$  operator. Since the  $a^2$  taste-splitting effect is in the square of the mass, the mass splitting between pseudoscalars actually falls as the mass increases (as long as the mass does not become too large) [2]. So in fact the difference in mass between the two tastes of  $D_s$  used here is very small, as we will see in Section IV.

For vector mesons taste-splittings are significantly smaller [9]. Here we will use both a local and a 1-link point-split operator for the  $\phi$  and discuss results from those and the comparison between them in IV A. In principle the effect of ‘disconnected’ diagrams (two  $s$  quark loops connected only by gluon exchange) to be small for vector mesons [15] and we do not include them here. In the real world the  $\phi$  decays strongly to  $K\bar{K}$  but not in our lattice QCD simulations. We consider the effect of that on our  $\phi$  mesons in Section IV A.

A schematic diagram for the 3-point function for  $D_s$  to  $\phi$  decay is shown in Fig. 2. Quark propagators 1 and 3 correspond to  $s$  quarks and propagator 2 is for a  $c$  quark. Propagators 1 and 3 are tied together with appropriate phases to make a  $\phi$  meson at the origin. Propagator 2 is calculated from a source made from propagator 1 at timeslice  $T$ , using appropriate phases for a pseudoscalar  $D_s$  meson. Finally propagators 2 and 3 are combined at timeslice  $t$  with appropriate phases to correspond to a vector, axial vector or pseudoscalar current, so that we can determine the vector and axial vector form factors discussed in Section II.

To cover the range of squared 4-momentum transfer,  $q^2$ , available in the decay we keep the  $D_s$  meson at rest and give spatial momentum to the  $\phi$  meson varying from zero up to an appropriate value to set  $q^2 = 0$ . We do this by calculating  $s$  quark propagators for propagator 3 that carry spatial momentum through the use of a ‘twisted boundary condition’ [16, 17]. If propagator 3 is calculated

with boundary condition

$$\chi(x + \hat{e}_j L) = e^{i\theta_j} \chi(x), \quad (9)$$

then the momentum of the  $\phi$  meson made by combining propagators 1 and 3 with our random wall sources and summing over spatial sites at the sink is

$$p_j = \frac{\theta_j}{L_s}. \quad (10)$$

The boundary condition in eq. (9) is actually implemented by multiplying the gluon links in the  $j$  direction by phase  $\exp(i\theta_j/L_s)$ .

The 3-point function for  $D_s \rightarrow \phi$  is calculated for all  $t$  values from 0 to  $T$  and for several values of  $T$  (which include both even and odd values as given in Table I) so that the dependence of the function on  $t$  and  $T$  can be fully mapped out. The 3-point function is fit simultaneously with the 2-point function using fit forms

$$\begin{aligned} C_{2pt}^{(P)} &= \sum_{i_n, i_o} \{d_{i_n}^{(P)}\}^2 \text{fn}(E_{i_n}^{(P)}, t') - \{\tilde{d}_{i_o}^{(P)}\}^2 \text{fo}(\tilde{E}_{i_o}^{(P)}, t') \\ C_{3pt}^{P \rightarrow Q} &= \sum_{i_n, j_n} d_{i_n}^{(P)} \text{fn}(E_{i_n}^{(P)}, t) J_{i_n, j_n}^{nn} d_{j_n}^{(Q)} \text{fn}(E_{j_n}^{(Q)}, T - t) \\ &\quad - \sum_{i_n, j_o} d_{i_n}^{(P)} \text{fn}(E_{i_n}^{(P)}, t) J_{i_n, j_o}^{no} \tilde{d}_{j_o}^{(Q)} \text{fo}(\tilde{E}_{j_o}^{(Q)}, T - t) \\ &\quad + (n \leftrightarrow o) \end{aligned} \quad (11)$$

with

$$\begin{aligned} \text{fn}(E, t) &= e^{-Et} + e^{-E(L_t - t)} \\ \text{fo}(E, t) &= (-1)^{t/a} \text{fn}(E, t). \end{aligned} \quad (12)$$

We use Bayesian methods [18] that allow us to include the effect of excited states, both ‘radial’ excitations ( $n$ ) and, because we are using staggered quarks, opposite parity mesons that give oscillating terms ( $o$ ). We fit all the 2-point and 3-point correlators on a given ensemble at multiple momenta simultaneously to take account of correlations. The Bayesian approach requires the constraint of prior values and widths on the parameters. These are taken as: ground-state energy, 2% width; splitting between ground-state and excited energies, 600 MeV with 50% width; splitting between ground-state and lowest oscillating state, 400 MeV with 50% width; amplitudes, 0.01(1.0) for normal states and 0.01(0.5) for oscillating states; matrix elements, 0.01(1.0).

In Eq. 11,  $d_{i_n}$  are the amplitudes for creation/annihilation of the  $D_s$  or  $\phi$  mesons. The amplitude can be converted into the decay constant and this will be discussed for the  $\phi$  in Section IV A. Results for the  $D_s$  mass and decay constant on these gauge configurations were presented in [8].  $J_{i_n, j_n}$  is related to the matrix element of the vector, axial vector or pseudoscalar current between  $D_s$  and  $\phi$ . By matching to a continuum correlator with a relativistic normalisation of states and allowing for a renormalisation of the lattice current we

see that the matrix elements between the ground state mesons that we want to determine are given by

$$\langle D_s | J | \phi \rangle = Z \sqrt{4E_0^{(D_s)} E_0^{(\phi)}} J_{0,0}^{nn}. \quad (13)$$

The vector current we use for the  $D_s \rightarrow \phi$  transition is a local spatial current. We use both a local and a point-split axial vector current. The point-split current does not include gauge links because we work in the Coulomb gauge. The local pseudoscalar current we use is absolutely normalised when multiplied by the lattice quark mass. The vector and axial vector currents are nonperturbatively normalised, as described in Appendix A, and the  $Z$  factors we obtain on each of our ensembles are given in Table V.

## IV. RESULTS

### A. The $\phi$ meson

When handling the  $\phi$  meson in our lattice QCD calculations we have treated it as a pure  $s\bar{s}$  vector meson and not included quark-line disconnected diagrams that could mix in light-quark components. These effects are expected to be very small from phenomenology. For example the width for  $\phi$  to decay to  $\pi^0\gamma$ , which would be zero for a pure  $s\bar{s}$   $\phi$ , is 5.5keV [19] (branching fraction 0.13%). This compares to a width to  $\pi^0\gamma$  for the light vector  $\omega$  of 700keV [19] (branching fraction 8%). In lattice QCD calculations where quark-line disconnected diagrams have been included they are indeed found to have tiny effect for vectors. Ref. [20] gives a mixing angle between  $\phi$  and  $\omega$  of  $1.7(2)^\circ$  for relatively heavy light quarks. We conclude that quark-line disconnected diagrams are a negligible issue here.

The  $\phi$  meson in the real world decays strongly to  $K\bar{K}$  and hence is not ‘gold-plated’. The  $\phi$  meson mass is close to threshold for this decay, however, and so the  $\phi$  width is small (4 MeV [19]). It may then be true that the impact of the decay channel is not large and it may effectively be possible to treat the  $\phi$  as being close to gold-plated within lattice QCD.

A simple model by which we can analyse the effect of the  $K\bar{K}$  channel on the  $\phi$  is to treat both  $\phi$  and  $K$  as elementary particles and couple them with a P-wave vertex,  $g\varepsilon \cdot p$ . Here  $\varepsilon$  is the polarization vector of the  $\phi$  and  $p$  is the momentum of the  $K$  in the  $\phi$  rest frame. Then, from perturbation theory treating the  $K$  as nonrelativistic

$$\Delta E_\phi = g^2 \int^\Lambda \frac{d^3p}{(2\pi)^3} \frac{|\varepsilon \cdot p|^2}{\Delta M - p^2/M_K + i\epsilon} \quad (14)$$

where  $\Delta M \equiv M_\phi - 2M_K$ . Spin-averaging, and absorbing factors into the coupling constant, gives

$$\begin{aligned} \Delta E_\phi &= \tilde{g}^2 \int_0^\Lambda dp \frac{p^4}{\gamma^2 - p^2 + i\epsilon} \\ &= \tilde{g}^2 \left( -\frac{\Lambda^3}{3} - \gamma^2 \Lambda - \frac{i\pi}{2} \gamma^3 \right) \end{aligned} \quad (15)$$

Set	$am_s$	$aM_{\eta_s}$	$aM_\phi(\gamma_\mu \otimes \gamma_\mu)$	$af_\phi/Z(\gamma_\mu \otimes \gamma_\mu)$	$aM_\phi(\gamma_\mu \otimes 1)$	$af_\phi/Z(\gamma_\mu \otimes 1)$
1	0.0489	0.4111(1)	0.6386(26)	0.1504(36)	0.6365(44)	0.1341(59)
2	0.0496	0.4163(1)	0.6549(31)	0.1571(41)	0.6569(28)	0.1401(30)
3	0.0337	0.2937(1)	0.4550(35)	0.1100(30)	0.4570(21)	0.1026(34)

TABLE II: For each ensemble we give the  $s$  valence quark masses and  $\eta_s$  meson mass in lattice units. These are followed by: (columns 4 and 5) the mass and bare (unrenormalised) decay constant for the local  $\phi$  and (columns 6 and 7) the mass and bare decay constant for the 1-link  $\phi$ .

dropping higher order terms in  $\gamma$  where  $\gamma^2 = (M_\phi - 2M_K)M_K$ . The imaginary part is the width,  $\Gamma_\phi = \tilde{g}^2 \pi \gamma^3$ , and we can use this to estimate  $\tilde{g}$ . Using the physical width and physical masses [19] gives  $\tilde{g}^2 \approx 0.35$  for both charged  $K$  and neutral  $K$  decay modes. The shift in the mass expected from coupling to the  $K$  decay mode is then  $-\tilde{g}^2 \gamma^2 \Lambda$ , giving a result of  $\approx -5\text{MeV}$ . This is a very small effect, less than 0.5% of the mass, so that the  $\phi$  meson behaves as a gold-plated particle to a good approximation.

On the lattice, the coupling to the  $K\bar{K}$  decay mode is distorted by the fact that the  $K$  meson will typically have a higher mass than its physical value because the sea  $u/d$  quarks will be too heavy. Then  $M_\phi - 2M_K$  will be negative and the expected shift in the  $\phi$  meson mass resulting from coupling to  $K\bar{K}$  will be positive. Thus we expect the  $\phi$  meson mass on the lattice to have more dependence on the sea  $u/d$  quark masses than a typical gold-plated meson would have, and for its mass to be too high for unphysically heavy  $u/d$  quark masses.

Both of these effects are borne out in our results. Table II gives results for the  $\phi$  mass obtained from the combined fit to 2-point and 3-point functions described in Eq. 11, along with values of the  $\eta_s$  meson mass for the same valence  $s$  quarks. Notice that the statistical error on the  $\phi$  mass is much larger than that for the  $\eta_s$ . This is a consequence of the exponentially falling signal-to-noise ratio for particles like the  $\phi$  where the noise amplitude is governed by a lighter mass (in this case the  $\eta_s$ ) than the signal. Figure 3 shows the difference in mass between the  $\phi$  and the  $\eta_s$  plotted as a function of the sea light quark mass in units of the physical strange quark mass (which is given in Table I). The figure shows results for the 1-link  $\phi$  operator but results for the local  $\phi$  are similar. The shaded band gives the result at the physical value of  $m_l/m_s$  ( $1/27.5$  [19]) from a simple fit. This allows for a linear term in  $m_l/m_s$  and quadratic and quartic terms in  $a$ . We obtain the result  $0.346(15)$  GeV at the physical point, which agrees within errors with the value obtained from the experimental result for the  $\phi$  mass and the lattice result for the  $\eta_s$  mass in the continuum and chiral limits [11] ( $0.3337(40)$  GeV). Hence it seems that light quark mass effects from the coupling to  $K\bar{K}$  are relatively benign compared to the significant statistical errors that we have in the  $\phi$  mass.

A similar result is seen for the  $\phi$  meson decay constant,  $f_\phi$ . Table II gives results for the  $\phi$  decay constant obtained from the combined fit to 2-point and 3-point

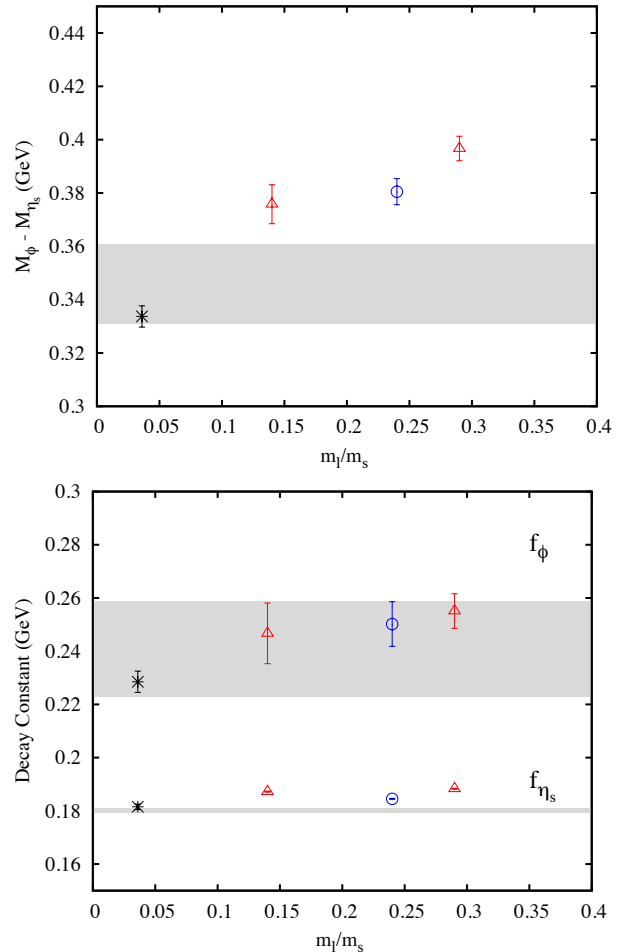


FIG. 3: Upper plot: The difference in mass between the  $s\bar{s}$  vector  $\phi$  and pseudoscalar  $\eta_s$  as a function of sea light quark mass in units of the physical strange quark mass for coarse lattices (red open triangles) and fine (green open circle). The ‘experimental’ result is plotted with a black burst. This is obtained from the experimental result for  $M_\phi$  and the lattice QCD result for  $M_{\eta_s}$  in the continuum and chiral limits [11]. The gray shaded band gives the lattice result in the continuum and chiral limits from a simple fit described in the text. Lower plot: A similar plot for the  $\phi$  and  $\eta_s$  decay constants. The black bursts denote the experimental result for the  $\phi$  obtained from its leptonic width [19] and the result from lattice QCD for the  $\eta_s$  [11].

functions described in Eq. 11. The decay constant is extracted from the amplitude of the ground-state  $\phi$  in the 2-point function,  $d_0^\phi$ , using

$$f_\phi = Z d_0^\phi \sqrt{\frac{2}{E_0^\phi}} \quad (16)$$

where  $Z$  is the renormalisation factor required to match the lattice vector current used to create or destroy the  $\phi$  to the continuum. We give results for both the local vector current and the 1-link vector current in Table II and they can both be renormalised fully nonperturbatively. How this is done is described in Appendix A and the appropriate renormalisation constants are given in Table V.

We plot  $f_\phi$  in Figure 3 for the 1-link  $\phi$ . Results for the local  $\phi$  are similar. A simple extrapolation, as for the mass, gives a physical result of  $f_\phi = 241(18)$  MeV, which agrees within errors with the experimental value of  $f_\phi = 229(4)$  MeV obtained from  $\Gamma(\phi \rightarrow e^+e^-)$  (1.27(4) keV [19]). The decay constant is related to the leptonic decay rate by

$$\Gamma(\phi \rightarrow e^+e^-) = \frac{4\pi}{3} \alpha_{QED}^2 e_s^2 \frac{f_\phi^2}{m_\phi}, \quad (17)$$

where  $e_s$  is the electric charge of the  $s$  quarks in units of  $e$ , i.e.  $-1/3$ . We show for comparison the results for the decay constant of the  $\eta_s$  which was studied on the lattice in [11]. There is some sign that the  $\phi$  meson has enhanced dependence on  $m_l/m_s$  compared to that of the gold-plated  $\eta_s$ . This might be expected to be a result of coupling to  $K\bar{K}$  but it causes no problem in the extrapolation to the physical point of the decay constant within the lattice errors of 7%.

For a phenomenological comparison that could shed light on how large an effect we might expect on meson properties from coupling to decay channels, we can compare the  $\omega$  and the  $\rho$ . They are both made of light  $u/d$  valence quarks but the  $\rho$  has a strong two-body decay mode to  $\pi\pi$  which is not allowed for the  $\omega$  by G-parity (which instead decays to three  $\pi$ ). The  $\omega$  and  $\rho$  masses nevertheless agree to within 10 MeV so little effect of the  $\rho$  decay mode is seen there. We expect the leptonic width of the  $\omega$  to be one-ninth that of the  $\rho$  simply from isospin [21]. In fact this expectation is violated by about 30%, which might indicate a 15% effect in the  $\rho$  decay constant from coupling to decay channels. This should be compared to a 7(7)% possible effect in the  $\phi$  from our results, as described above.

For possible effects on a meson to meson transition rate where one of the mesons in the process is gold-plated and the other is not, we can compare the decay of  $\rho$  and  $\omega$  to  $\pi^0\gamma$ . Here we expect the rate for the  $\rho$  to be one-ninth that of the  $\omega$  [21]. This expectation is violated by 12%, indicating a possible 6% effect in the matrix element. Following the discussion of the decay constant above, this would mean that a reasonable error to take

on a transition matrix element involving the  $\phi$  (i.e.  $D_s \rightarrow \phi l\nu$ ) as a result of  $\phi$  coupling to  $K\bar{K}$  might be half this, i.e. 3%.

## B. Results for form factors

As discussed in Section III we calculate 3-point functions for  $D_s$  to  $\phi$  decay by inserting either a vector, axial vector or pseudoscalar current between the  $D_s$  and the  $\phi$ . By choosing appropriate kinematic conditions we can isolate the individual form factors from Eq. 1. We keep the  $D_s$  meson at rest but can give the  $\phi$  spatial momentum in different directions and choose its spin polarization.

For a 3-point function made of staggered quarks all the tastes must ‘cancel’. Therefore only certain tastes of current can be used with certain tastes of mesons. Below we discuss each of the form factors we extract, explaining the method used. The  $Z$  factors for all of the different currents are determined fully non-perturbatively and we describe how that is done in Appendix A. Table III collects all of the form factor results.

### 1. Determining $A_1(q^2)$

From Eq. 1 we see that  $A_1(q^2)$  is the only form factor that appears in the matrix element of the axial vector current when  $\varepsilon^* \cdot q = 0$ , i.e. when the  $\phi$  polarization is orthogonal to the momentum transfer. This is the only contribution to the matrix element at  $q_{max}^2$  when the final state  $\phi$  meson is at rest. To calculate  $A_1(q^2)$  away from  $q_{max}^2$ , we give the  $\phi$  meson momentum in an orthogonal spatial direction to its polarization.

When the kinematics are set up such that  $\varepsilon^* \cdot q = 0$ , the transition matrix element becomes

$$\langle \phi(p', \varepsilon) | A^\mu | D_s(p) \rangle = (m_{D_s} + m_\phi) \varepsilon^{*\mu} A_1(q^2). \quad (18)$$

The  $\phi$  polarization vector and the axial vector current must then be in the same spatial direction so that the matrix element in Eq. 18 is non-vanishing.

There is a choice of operators that can be used to extract  $A_1(q^2)$ : either using a local vector operator for the  $\phi$  and local axial vector for the current or a 1-link vector and 1-link axial vector.

If we use the 1-link  $\phi$  with spin-taste  $\gamma_\mu \otimes 1$  at time 0, we also use the 1-link axial vector with spin-taste  $\gamma_5 \gamma_\mu \otimes \gamma_5$  at  $t$  and the local pseudoscalar ( $\gamma_5 \otimes \gamma_5$ ) for the  $D_s$  at  $T$  (see Fig. 2). The staggered 3-point correlator is then

$$C_{3pt}(0, t, T) = \sum_{x,y,z} (-1)^{x_\mu + y_\mu} \varepsilon(x) \varepsilon(z) \quad (19) \\ \times \text{Tr} [g_s(x, z) g_c(z, y) g_s^{\theta\dagger}(x \pm \hat{\mu}, y \pm \hat{\mu})],$$

where the sites  $x, y$  and  $z$  are at times 0,  $t$  and  $T$  and the sum is over the timeslice. For the point-splitting at  $x$  and  $y$  we average over links in the forward and backward

Set	Form factor	T values	$am_{D_s}$	$\theta$	$aE_\phi$	$a^2q^2$	$F(q^2)$
1	Local $A_1(q^2)$	12,15,18	1.1889(1)	0.0	0.6386(26)	0.303(3)	0.685(8)
1	Local $A_1(q^2)$	12,15,18	1.1889(1)	7.0	0.7108(40)	0.143(4)	0.657(12)
1	Local $A_1(q^2)$	12,15,18	1.1889(1)	10.18	0.7817(62)	-0.014(5)	0.624(22)
1	1-link $A_1(q^2)$	12,15,18	1.1889(1)	0.0	0.6365(44)	0.305(6)	0.694(17)
1	1-link $A_1(q^2)$	12,15,18	1.1889(1)	7.0	0.7056(51)	0.148(5)	0.648(25)
1	1-link $A_1(q^2)$	12,15,18	1.1889(1)	10.18	0.7815(82)	-0.014(6)	0.642(34)
1	$A_0(q^2)$	12,15,18	1.1889(1)	7.0	0.7090(35)	0.145(3)	0.808(24)
1	$A_0(q^2)$	12,15,18	1.1889(1)	10.18	0.7784(51)	-0.011(4)	0.707(23)
1	$A_2(q^2)$	12,15,18	1.1889(1)	7.0	0.7090(35)	0.145(3)	0.529(106)
1	$A_2(q^2)$	12,15,18	1.1889(1)	10.18	0.7784(51)	-0.011(4)	0.430(90)
1	$V(q^2)$	12,15,18	1.1909(5)	7.0	0.7121(41)	0.144(3)	1.141(72)
1	$V(q^2)$	12,15,18	1.1909(5)	10.18	0.7853(61)	-0.015(5)	1.055(69)
2	Local $A_1(q^2)$	12,15,18	1.2015(1)	0.0	0.6549(31)	0.298(3)	0.689(13)
2	Local $A_1(q^2)$	12,15,18	1.2015(1)	6.0	0.7195(56)	0.142(5)	0.627(26)
2	Local $A_1(q^2)$	12,15,18	1.2015(1)	8.39	0.7769(72)	0.004(6)	0.596(28)
2	1-link $A_1(q^2)$	12,15,18	1.2015(1)	0.0	0.6569(28)	0.296(3)	0.684(11)
2	1-link $A_1(q^2)$	12,15,18	1.2015(1)	6.0	0.7246(54)	0.137(5)	0.627(23)
2	1-link $A_1(q^2)$	12,15,18	1.2015(1)	8.39	0.7713(100)	0.009(9)	0.582(42)
2	$A_0(q^2)$	12,15,18	1.2015(1)	6.0	0.7151(49)	0.146(5)	0.787(29)
2	$A_0(q^2)$	12,15,18	1.2015(1)	8.39	0.7825(48)	-0.001(4)	0.701(22)
2	$A_2(q^2)$	12,15,18	1.2015(1)	6.0	0.7151(49)	0.146(5)	0.475(183)
2	$A_2(q^2)$	12,15,18	1.2015(1)	8.39	0.7825(48)	-0.001(4)	0.345(107)
2	$V(q^2)$	12,15,18	1.2040(3)	6.0	0.7176(67)	0.146(6)	1.116(87)
2	$V(q^2)$	12,15,18	1.2040(3)	8.39	0.7738(82)	0.009(7)	1.057(180)
3	Local $A_1(q^2)$	16,19,20,23	0.8460(1)	0.0	0.4550(35)	0.153(3)	0.717(23)
3	Local $A_1(q^2)$	16,19,20,23	0.8460(1)	6.0	0.5007(34)	0.073(2)	0.635(12)
3	Local $A_1(q^2)$	16,19,20,23	0.8460(1)	8.39	0.5563(54)	0.000(3)	0.648(23)
3	1-link $A_1(q^2)$	16,19,20,23	0.8460(1)	0.0	0.4570(21)	0.151(2)	0.716(11)
3	1-link $A_1(q^2)$	16,19,20,23	0.8460(1)	6.0	0.5038(33)	0.071(2)	0.658(14)
3	1-link $A_1(q^2)$	16,19,20,23	0.8460(1)	8.39	0.5463(43)	0.000(6)	0.638(18)
3	$A_0(q^2)$	16,19,20,23	0.8460(1)	6.0	0.4960(54)	0.076(4)	0.783(51)
3	$A_0(q^2)$	16,19,20,23	0.8460(1)	8.39	0.5523(20)	-0.003(1)	0.689(12)
3	$A_2(q^2)$	16,19,20,23	0.8460(1)	6.0	0.4960(54)	0.076(4)	0.499(181)
3	$A_2(q^2)$	16,19,20,23	0.8460(1)	8.39	0.5523(20)	-0.003(1)	0.553(80)
3	$V(q^2)$	16,19,20,23	0.8464(5)	6.0	0.5072(35)	0.069(2)	1.101(123)
3	$V(q^2)$	16,19,20,23	0.8464(5)	8.39	0.5468(55)	0.000(3)	1.128(104)

TABLE III: The form factor results for  $D_s \rightarrow \phi$  on each ensemble at all values of  $q^2$  calculated. Column 2 denotes the form factor for the result in column 8. The axial form factors are fitted simultaneously so the (Goldstone)  $D_s$  mass is the same for all of them on the same ensemble. The vector form factor  $V(q^2)$  instead is calculated using the non-Goldstone  $D_s$ . Columns 5 and 6 give the value of  $\theta$  used to give momentum to the  $\phi$  and the fitted  $\phi$  energy at this momentum.

directions. As the propagators are for staggered quarks, the trace is only over colour indices.

We write the staggered phase factors using  $\varepsilon(x) = \prod_\nu (-1)^{x_\nu}$ ,  $x_\mu^< = \sum_{\nu < \mu} x_\nu$ ,  $x_\mu^> = \sum_{\nu > \mu} x_\nu$  and  $\bar{x}_\mu = \sum_{\nu \neq \mu} x_\nu$ .

We fit the 3-point correlator simultaneously with the appropriate 2-point correlators. In this case, these are the correlators for the Goldstone  $D_s$  and 1-link  $\phi$ , given by

$$C_{2pt,D_s}(0,t) = \sum_{x,y} \text{Tr} [g_c(x,y)g_s^\dagger(x,y)] \quad (20)$$

and

$$C_{2pt,\phi}(0,t) = \sum_{x,y} \varepsilon(x)\varepsilon(y)(-1)^{x_\mu^<+y_\mu^<} \times \text{Tr} [g_s(x,y)g_s^{\theta\dagger}(x \pm \hat{\mu}, y \pm \hat{\mu})]. \quad (21)$$

The sites  $x$  and  $y$  are again at times 0 and  $t$ . The results using these correlators are called ‘1-link  $A_1(q^2)$ ’ in Table III.

If we use local operators, we have a  $\gamma_\mu \otimes \gamma_\mu$  operator at 0 for the  $\phi$ , a  $\gamma_\mu \gamma_5 \otimes \gamma_\mu \gamma_5$  axial vector at  $t$  and the local pseudoscalar at  $T$ . This gives the staggered 3-point correlation function

$$C_{3pt}(0,t,T) = \sum_{x,y,z} (-1)^{x_\mu+\bar{y}_\mu} \varepsilon(z) \times \text{Tr} [g_s(x,z)g_c(z,y)g_s^{\theta\dagger}(x,y)]. \quad (22)$$

The corresponding  $D_s$  2-point correlator is that given by Eq. 20 and the local  $\phi$  correlator is

$$C_{2pt,\phi}(0,t) = \sum_{x,y} (-1)^{x_\mu+y_\mu} \quad (23)$$

$$\times \text{Tr} [g_s(x,y)g_s^{\theta\dagger}(x,y)].$$

The determination of  $A_1(q^2)$  using a local axial current is called ‘Local  $A_1(q^2)$ ’ in Table III. The two determinations of  $A_1(q^2)$  should agree with one another, as the current operators and  $\phi$  mesons only differ by taste. Doing the calculation in two different ways allows us to test the differences between different tastes of staggered mesons in meson transitions. Agreement is seen in the results for  $A_1(q^2)$  given in Table III within our statistical errors. We find smaller statistical errors for Local  $A_1(q^2)$  on the coarse lattices (sets 1 and 2), so it is used for the final results.

### 2. Determining $A_0(q^2)$

The  $A_0(q^2)$  form factor can be related to the pseudoscalar density using the PCAC relation so can be extracted from the pseudoscalar matrix element using Eq. 3.

The staggered 3-point correlator calculated on the lattice then has  $\gamma_5 \otimes \gamma_5$  at both  $t$  and  $T$  and a 1-link  $\phi$  with spin-taste  $\gamma_\mu \otimes 1$  at 0. The correlator is

$$C_{3pt}(0,t,T) = i \sum_{x,y,z} (-1)^{x_\mu} \varepsilon(x)\varepsilon(y)\varepsilon(z) \quad (24)$$

$$\times \text{Tr} [g_s(x,z)g_c(z,y)g_s^{\theta\dagger}(x \pm \hat{\mu}, y)].$$

It cannot be calculated at rest because  $\varepsilon^* \cdot q$  must be non-zero for the matrix element to be non-zero. The  $\phi$  meson therefore carries momentum in the same direction as its polarization. We fit the 3-point correlators generated using Eq. 24 simultaneously with  $D_s$  and  $\phi$  2-point correlators as given in Eqs. 20 and 21. The results are given in Table III.

### 3. Determining $A_2(q^2)$

The form factor  $A_2(q^2)$  is difficult to calculate as it only contributes to the matrix element when  $\varepsilon^* \cdot q \neq 0$ . This requires the  $\phi$  meson’s polarization,  $\varepsilon^*$ , and momentum,  $p'$ , to be in the same direction. In this case, all of the axial form factors,  $A_1(q^2)$ ,  $A_2(q^2)$  and  $A_0(q^2)$ , appear and we calculate  $A_2(q^2)$  given  $A_1(q^2)$  and  $A_0(q^2)$ .

At  $q^2 = 0$ , we have a relationship between  $A_0$ ,  $A_1$  and  $A_2$  because  $A_3$  is given in terms of  $A_1$  and  $A_2$  by Eq. 2 and  $A_3(0) = A_0(0)$ . This means we can extract  $A_2(0)$  from the values of  $A_1(0)$  and  $A_0(0)$ .

Away from  $q^2 = 0$ , we no longer have the relation between  $A_0(q^2)$  and  $A_3(q^2)$  so extracting  $A_2(q^2)$  is more

complicated. If we calculate the 3-point correlation function given by Eq. 19, but with the  $\phi$  polarization,  $\varepsilon^*$ , parallel to its momentum,  $p'$ , the result depends of all the axial form factors, and is given by Eq. 1. Using the values of  $A_1(q^2)$  and  $A_0(q^2)$  determined as described in Sections IV B 1 and IV B 2,  $A_2(q^2)$  can be extracted. The results given in Table III use the local determination of  $A_1(q^2)$  to extract  $A_2(q^2)$ , but agree with using 1-link  $A_1(q^2)$ .

### 4. Determining $V(q^2)$

The vector form factor,  $V(q^2)$ , is the same form factor that appears in electromagnetic vector to pseudoscalar meson transitions, such as  $J/\psi \rightarrow \eta_c \gamma$  [9]. The form factor can be calculated with staggered quarks using the same 3-point correlator setup we used for  $J/\psi \rightarrow \eta_c \gamma$ .

We calculate  $V(q^2)$  using the non-Goldstone  $D_s$  and a 1-link vector operator for the  $\phi$  where the point-splitting is in a different spatial direction to the polarization. In spin-taste notation, this operator is  $\gamma_\mu \otimes \gamma_\mu \gamma_\nu$  and it is placed at time 0. As the  $D_s$  meson is at rest, the  $\phi$  must carry non-zero momentum. The non-Goldstone  $D_s$  at time  $T$  is simulated using a  $\gamma_5 \gamma_t \otimes \gamma_5 \gamma_t$  operator and there is a local  $\gamma_\alpha \otimes \gamma_\alpha$  vector operator at  $t$ . The 3-point correlation function is

$$C_{3pt}(0,t,T) = i \sum_{x,y,z} (-1)^{x_\nu} \varepsilon^{\nu+x_\mu+y_\alpha+z_t} \quad (25)$$

$$\times \text{Tr} [g_s(x,z)g_c(z,y)g_s^{\theta\dagger}(x \pm \hat{\nu}, y)].$$

The corresponding non-Goldstone  $D_s$  2-point function is given by

$$C_{2pt,D_s}(0,t) = \sum_{x,y} (-1)^{\bar{x}_t+\bar{y}_t} \times \text{Tr} [g_c(x,y)g_s^\dagger(x,y)] \quad (26)$$

and the  $\phi$  2-point correlator by

$$C_{2pt,\phi}(0,t) = \sum_{x,y} (-1)^{x_\nu} \varepsilon^{\nu+x_\mu+y_\nu+y_\mu} \quad (27)$$

$$\times \text{Tr} [g_s(x,y)g_s^{\theta\dagger}(x \pm \hat{\nu}, y \pm \hat{\nu})].$$

As the 3-point correlator must be a taste-singlet overall,  $\mu, \nu$  and  $\alpha$  must be three different spatial directions. The  $\phi$  meson polarization vector, vector current and  $\phi$  momentum must also all be orthogonal to one another due to the  $\epsilon^{\mu\nu\alpha\beta}$  in Eq. 1. Therefore the momentum of the  $\phi$  must be in the  $\nu$  direction. For the vector form factor, Eq. 1 reduces to

$$\langle \phi(p', \varepsilon) | V_\alpha | D_s(p) \rangle = \frac{2i\epsilon_{\alpha\mu\nu t}}{M_{D_s} + M_\phi} \varepsilon^{*\mu} p'^\nu p^t V(q^2). \quad (28)$$

As the  $D_s$  meson is at rest, only the time component of its 4-momentum is non-zero so Equation 28 must include  $p_t$ , the  $D_s$  energy (in this case, mass). We give our results for  $V(q^2)$  in Table III.

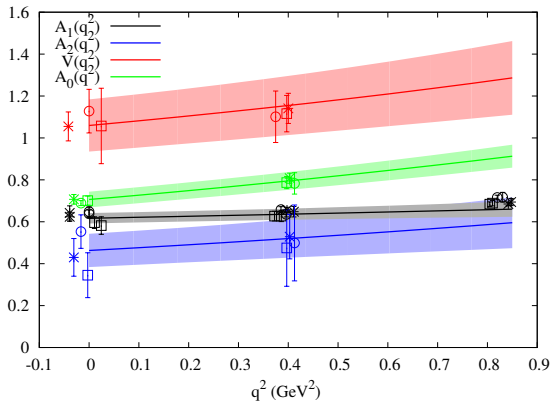


FIG. 4: Lines and bands show the form factors from our lattice QCD calculation extrapolated to the physical point as a function of  $q^2$  for  $q^2 = 0$  to  $q_{max}^2$ . The form factor  $A_1(q^2)$  is shown in black,  $A_2(q^2)$  in blue,  $V(q^2)$  in red and  $A_0(q^2)$  in green. We also plot the raw lattice results from Table III for each form factor. The bursts are the lattice data from Set 1, squares from Set 2 and circles Set 3. At  $q_{max}^2$ , the  $\phi$  meson is at rest and only  $A_1(q^2)$  contributes to the decay. We plot the lattice data for both the local and 1-link determinations of  $A_1(q^2)$ .

#### 5. Comparing form factors to experiment

We fit the correlators for all the axial form factors at all values of  $q^2$  simultaneously on each ensemble. This allows us to use the correlation matrix between them in our physical extrapolation. The results in Table III are taken from fits with 5 exponentials for Sets 1 and 2 and 4 exponentials for Set 3.

The extrapolation of the form factors to zero lattice spacing and physical light quark masses is more complicated than for meson masses and decay constants since we want to determine the functional form as a function of  $q^2$ . It is convenient to parameterise the form factors using the  $z$ -expansion [22–24]. The conversion from  $q^2$  to  $z$  is made using the transformation

$$z(q^2) = \frac{\sqrt{t_+ - q^2} - \sqrt{t_+ - t_0}}{\sqrt{t_+ - q^2} + \sqrt{t_+ - t_0}}, \quad (29)$$

where  $t_+ = (m_{D_s} + m_\phi)^2$ . We will use  $t_0 = 0$  here which means that  $z = 0$  corresponds to  $q^2 = 0$ . The  $z$ -expansion maps the line above the real axis from  $q^2 = \infty$  to  $q^2 = t_+$  and then back below the real axis to  $\infty$  onto the unit circle. The semileptonic region  $0 < q^2 < q_{max}^2 = t_- = (m_{D_s} - m_\phi)^2$  is then mapped to a line inside this circle. The shape of the form factor can be described by a power series in  $z$ . As  $z$  is small, the series can be truncated and the form factor described with only a few terms.

Physical particles of  $c\bar{s}$  quark content that have appropriate quantum numbers for that form factor and masses between  $t_+$  and  $t_-$  will appear as poles inside the unit

Form factor	Ratio
$A_1(0) = 0.615(24)$	–
$A_2(0) = 0.457(78)$	$r_2 = 0.74(12)$
$A_0(0) = 0.706(37)$	$r_0 = 1.14(6)$
$V(0) = 1.059(124)$	$r_V = 1.72(21)$

TABLE IV: The form factors calculated on the lattice at maximum recoil. For all the form factors other than  $A_1$ , we also give the ratio of the form factor at  $q^2 = 0$  to  $A_1(0)$ .

circle. We therefore remove those before we transform to  $z$ -space:

$$\tilde{A}_i(q^2) = \left(1 - \frac{q^2}{M_{D_{s1}}^2}\right) A_i(q^2) \quad (30)$$

and

$$\tilde{V}(q^2) = \left(1 - \frac{q^2}{M_{D_s^*}^2}\right) V(q^2). \quad (31)$$

The pole masses are  $M_{D_s^*} = 2112$  MeV for the vector and  $M_{D_{s1}} = 2459$  MeV for the axial vector [19]. The pole factors here are relatively benign because  $\sqrt{q_{max}^2}$  for  $D_s \rightarrow \phi$  decay is much smaller than either of these masses. This is also the reason why we only divide out one pole in each case, and do not consider higher mass particles. The  $z$ -expansion can then be used to extrapolate the lattice QCD form factors to the physical limit by making the coefficients of the terms in  $z$ -space depend on the lattice spacing and sea quark masses [1, 25].

For each of the form factors,  $\tilde{F}(z)$ , we use the fit function

$$\tilde{F}(z) = \sum_{n=0}^3 B_n^F \{1 + C_n^F a^2 + D_n^F a^4 + E_n^F x_l\} z^n. \quad (32)$$

The fit parameter  $B_0^F$  is the form factor at  $z = q^2 = 0$  and chiral parameter  $x_l = m_l/m_{s,phys}$  is given in Table I. We include up to  $n = 3$  in our fit as we find that all higher terms make no difference to the results.

All the form factors are fitted together to this form, but the coefficients are independent for each one. The priors are taken as 0.0(2.0) for  $B_n^F$  ( $n > 0$ ) and 0.0(1.0) for  $C_n^F$ ,  $D_n^F$  and  $E_n^F$ . The priors for the form factors at  $z = 0$  are  $B_0^{A_1} = 0.6(0.2)$ ,  $B_0^{A_2} = 0.4(0.2)$ ,  $B_0^V = 1.0(0.2)$  and  $B_0^{A_0} = 0.7(0.2)$ . As the values of the form factors at  $q^2 = 0$  are given by fit parameters, we can enforce the kinematic constraint  $A_3(0) = A_0(0)$  by replacing  $B_0^{A_0}$  with  $\frac{M_{D_s} + M_\phi}{2M_\phi} B_0^{A_1} - \frac{M_{D_s} - M_\phi}{2M_\phi} B_0^{A_2}$ . This does not significantly alter the results obtained from our fit, since they are consistent with the constraint without imposing it. The physical  $z$ -expansion of the form factor is obtained by setting  $a = 0$  and  $x_l = 1/27.5$  [19].

After the extrapolation, the form factors in the physical limit are converted back to  $q^2$  space. We plot the

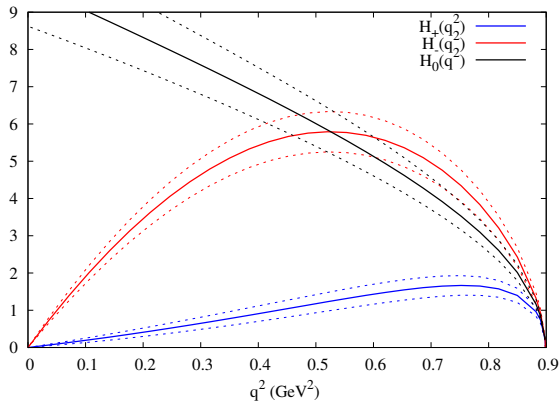


FIG. 5: The  $D_s \rightarrow \phi l \nu$  helicity amplitudes constructed from our extrapolated form factors. They are shown as  $p_\phi q^2 |H_\pm(q^2)|^2$  and  $p_\phi q^2 |H_0(q^2)|^2$ , including the kinematic factors that appear in the differential decay rate. At the  $q^2 = q_{max}^2$  end of the distribution,  $p_\phi \rightarrow 0$  and each of the helicity amplitudes vanishes.

$A_1(q^2)$ ,  $A_0(q^2)$ ,  $A_2(q^2)$  and  $V(q^2)$  form factors against  $q^2$  for the full physical range of  $q^2$  values in Figure 4. The solid lines are the central values of the form factors after the extrapolation and the shaded bands show the errors. The raw lattice results for each of these form factors are also plotted with symbols in Figure 4. We see that the form factors agree well on each set of gauge configurations and do not vary significantly with lattice spacing or sea quark masses, so the extrapolation to the physical point changes the results very little.

Our results are most accurate for the  $A_1$  form factor. In Table IV we give our values for each form factor at  $q^2 = 0$  and its ratio to the  $A_1$  form factor at that point. The ratios can be compared to experimental results from BaBar [4] who quote  $r_V = V(0)/A_1(0) = 1.849(60)(95)$  and  $r_2 = A_2(0)/A_1(0) = 0.763(71)(65)$ . We find  $r_V = 1.72(21)$  and  $r_2 = 0.74(12)$ , in agreement with experiment. We can also take the ratio  $r_0 = A_0(0)/A_1(0)$  on the lattice and we find  $r_0 = 1.14(6)$ . The error in the lattice QCD results is dominated in all cases by the statistical error in the raw lattice results.

To extract the differential decay rate from Eq. 4, we need to combine the form factors into the helicity amplitudes given in Eqs. 5 and 6. The helicity amplitudes appear in Eq. 4 as  $p_\phi q^2 |H_i(q^2)|^2$ , so we plot this combination as a function of  $q^2$  in Figure 5 for  $H_\pm(q^2)$  and  $H_0(q^2)$ . In Figure 5, we include a multiplying factor of  $\frac{32}{9}$  from the angular integration; the factor is the same for each helicity. This means we are plotting the contribution to the differential decay rate as a function of  $q^2$  for each helicity. The cross terms between different helicity amplitudes in Eq. 4 vanish when we integrate over the angle  $\chi$  so these only affect the distribution in  $\chi$ , and not in  $q^2$ . At low  $q^2$ , the decay rate is dominated by  $H_0(q^2)$ . Throughout the range of  $q^2$ , both  $H_0(q^2)$  and  $H_-(q^2)$  contribute more than  $H_+(q^2)$ , as expected from

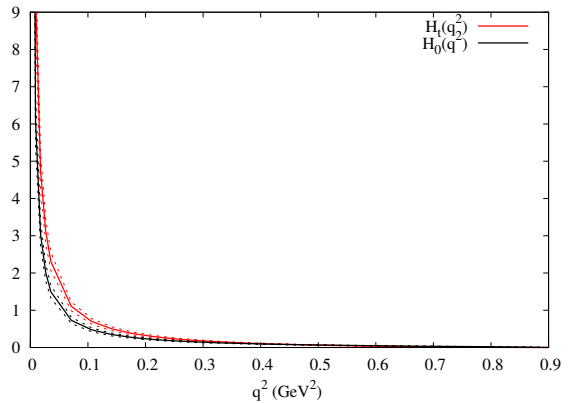


FIG. 6: Helicity amplitude contributions to  $D_s \rightarrow \phi l \nu$  which are suppressed by the lepton mass. Here we plot the contributions from  $H_0(q^2)$  and  $H_t(q^2)$  which are enhanced at small values of  $q^2$ . They are plotted as they appear in the differential decay rate for muons, i.e.  $m_\mu^2 p_\phi |H_i(q^2)|^2$ . The scale is the same as in Figure 5. For semileptonic decay with electrons in the final state, these contributions are further suppressed.

the  $V - A$  nature of the weak interaction. As we plot the combination  $p_\phi q^2 |H_i(q^2)|^2$ , all the helicity amplitudes go to zero at  $q_{max}^2$  because  $p_\phi = 0$  in this limit.

The terms which are suppressed by the lepton mass appear in the differential decay rate as  $m_\ell^2 p_\phi |H_i(q^2)|^2$  and the largest contributions come from  $H_t(q^2)$  and  $H_0(q^2)$  which are enhanced at low values of  $q^2$ . In Figure 6, we plot these contributions as  $m_\mu^2 p_\phi |H_i(q^2)|^2$ , again including factors from the angular integrals, so that these can be compared directly with Figure 5. The scale is the same and shows that these contributions are only large at small values of  $q^2$ . The decay  $D_s \rightarrow \phi \mu \nu$  has been studied by FOCUS [26]. Here we compare our results in most detail to those of BaBar [4] who measured the rate for  $D_s \rightarrow \phi e \nu$ . For electrons in the final state, the contributions shown in Figure 6 are smaller by a factor of  $m_e^2/m_\mu^2$  ( $=2 \times 10^{-5}$ ) and will not be visible.

## 6. Determining $V_{cs}$

The differential decay rate for  $D_s \rightarrow \phi l \nu$  is given by Eq. 4 and we can plot it as a function of each of  $q^2$ ,  $\cos \theta_K$ ,  $\cos \theta_\ell$  and  $\chi$  by integrating over the other three. The angular integrals are straightforward and we integrate over  $q^2$  numerically. The distributions we obtain from our form factors are plotted in Figure 7, where we take the value of  $V_{cs}$  from unitarity and use  $\mathcal{B}r(\phi \rightarrow K^+ K^-) = 0.489(6)$  [19]. Our lattice results are plotted as red data points with errors and the experimental results from BaBar [4] are plotted as the blue histogram. To avoid the effects of experimental cuts on the distributions (particularly on the lepton momentum), we reconstruct the decay rate in each bin from the results quoted by BaBar for the ratios of form factors at  $q^2 = 0$

and the pole masses for the  $q^2$  distributions they obtain from fits to their data. The experimental errors are not plotted, but they are of a similar size to our lattice errors. There is good agreement between the lattice results and experiment both in magnitude and shape for each of the differential distributions. We discuss the different distributions one by one below.

After performing the angular integrals, all of the helicity factors,  $|H_+(q^2)|^2$ ,  $|H_-(q^2)|^2$  and  $|H_0(q^2)|^2$  have the same coefficient in the  $q^2$  distribution. The relative contribution of each one as a function of  $q^2$  is then as shown by Figure 5.

The  $\cos\theta_\ell$  distribution is dominated by  $H_0$  at  $\cos\theta_\ell = 0$ .  $|H_0|^2$  appears with a factor of  $(1 - \cos^2\theta_\ell)$  so makes no contribution at the  $\cos\theta_\ell = \pm 1$  ends of the distribution. At  $\cos\theta_\ell = 1$ , the only helicity that contributes is  $H_+$  and at  $\cos\theta_\ell = -1$ , only  $H_-$  contributes as these helicity amplitudes appear with factors  $(1 \pm \cos\theta_\ell)^2$ . We see that the distribution is larger at  $\cos\theta_\ell = -1$  than  $+1$ , which is a result of the dominance of  $H_-$  over  $H_+$  coming from the  $V - A$  weak interaction.

The helicities  $H_\pm$  both contribute to the  $\cos\theta_K$  distribution as  $1 - \cos^2\theta_K$  and dominate at  $\cos\theta_K = 0$ . At  $\cos\theta_K = \pm 1$ , the only contribution is from  $H_0$ , which contributes as  $\cos^2\theta_K$ . The coefficients from the integrals over  $\cos\theta_\ell$  and  $\chi$  are  $\frac{16}{3}$  for  $|H_0|^2$  and  $\frac{8}{3}$  for  $|H_+|^2 + |H_-|^2$ .

The  $\chi$  distribution is a constant with an oscillation of  $-\cos 2\chi H_+(q^2)H_-(q^2)$  as the  $H_0(q^2)H_\pm(q^2)$  terms in Eq. 4 vanish when we integrate over the other angles.

By integrating over all of the kinematic variables, we can calculate the total decay rate. We can then extract  $V_{cs}$  by comparing the total decay rate to that measured by BaBar in [4]. We take BaBar's branching ratio for  $D_s \rightarrow \phi e^+ \nu_e$  of  $2.61(17) \times 10^{-2}$  and  $\tau_{D_s} = 500(7) \times 10^{-15} \text{ s}$  [19]. The experimental measurements and lattice calculation differ by a factor of  $|V_{cs}|^2$  so we obtain  $V_{cs} = 1.017(44)_{\text{latt}}(35)_{\text{expt}}(30)_{K\bar{K}}$ . The error from lattice QCD includes statistical errors from the lattice data (which dominate), uncertainty in the determination of the weak current  $Z$  factors and the extrapolation to the physical point. The final error takes into account the fact that the  $\phi$  meson has a strong decay mode to  $K\bar{K}$ . As discussed in Section IV A, we estimate this error to be 3%. This gives us a final result of  $V_{cs} = 1.017(63)$ .

This value is in agreement with unitarity [19] and other lattice measurements of  $V_{cs}$  from  $D_s$  leptonic [8] decay and  $D \rightarrow K\ell\nu$  semileptonic [1] decay.

## V. DISCUSSION

For pseudoscalar to pseudoscalar meson transitions, we have found that the form factors agree for  $D \rightarrow K$  and  $D_s \rightarrow \eta_s$  to within 2% [1]. These decays differ only by whether the spectator quark in the decay is a light or strange quark. To test whether the same is true for the pseudoscalar to vector transitions, we can compare the form factors we extract for  $D_s \rightarrow \phi$  with experimental

results for  $D \rightarrow K^*$ .

CLEO [6] give their reconstructed values of  $q^2 |H_i(q^2)|^2$  for  $i = \pm, 0$  in  $q^2$  bins. We construct the  $D \rightarrow K^*$  helicity amplitudes from Eqs. 5 and 6, using the same form factors as  $D_s \rightarrow \phi$  and replacing the meson masses and kinematic factors with those appropriate for  $D \rightarrow K^*$ .

In Figure 8, we plot  $q^2 H_i^2(q^2)$  for  $H_\pm$  and  $H_0$ . The lattice data is plotted in red and CLEO's results are in black. The final red point is offset slightly from experiment – it is at  $q_{max}^2 = 0.954 \text{ GeV}^2$ . The CLEO data is normalised by  $q^2 |H_0(q^2)|^2 \rightarrow 1$  as  $q^2 \rightarrow 0$ , so we apply the same normalisation condition to the lattice results.

There is reasonable agreement between lattice and experiment, which indicates that the semileptonic form factors for  $D_s \rightarrow \phi$  and  $D \rightarrow K^*$  also show little dependence on the spectator quark mass. However, the comparison between the  $D_s \rightarrow \phi$  and  $D \rightarrow K^*$  decays may be further complicated by the vector particles' widths. We have treated the  $\phi$  meson as stable in our calculation of the semileptonic form factors and take a systematic error, as described in Section IV A, to account for this. The width of the  $K^*$  is considerably larger than that of the  $\phi$  and this may have a larger effect on the  $D \rightarrow K^* \ell \nu$  decay, limiting the extent to which we can expect it to be well described by the  $D_s \rightarrow \phi \ell \nu$  form factors we have calculated. This strong decay mode also makes it difficult to calculate  $D \rightarrow K^*$  form factors directly to high accuracy in lattice QCD.

We do not compare the results for  $H_t(q^2)$  because the experimental errors are too large. However, CLEO are able to use the ratio of semileptonic decays to electrons and muons to extract information about the lepton-mass-suppressed helicity functions. This is encouraging for a future comparison of these helicity functions between lattice QCD and experiment.

## VI. CONCLUSIONS

We have calculated the complete set of axial vector and vector form factors for a pseudoscalar to vector weak semileptonic decay from full lattice QCD for the first time. We chose the process  $D_s \rightarrow \phi \ell \nu$  because the initial and final mesons contain no valence light quarks and so we can do a relatively accurate calculation. We are also able to cover the full range of  $q^2$  available to the decay. Calculating all of the form factors allows us to construct the angular decay distributions which contain information about the helicity of the  $W$  boson because the final state particle is a vector. The distributions we obtain are in good agreement with those observed by experiment.

Comparison of the total rate, integrated over all kinematic variables, with the experimentally measured branching fraction allows us to extract a value for the CKM element  $V_{cs}$ . Our final result for  $V_{cs}$  is  $1.017(44)_{\text{latt}}(35)_{\text{expt}}(30)_{K\bar{K}}$ . In Figure 9, we compare this value with those from the lattice determination of the  $D_s$  decay constant and its comparison to  $D_s$  leptonic de-

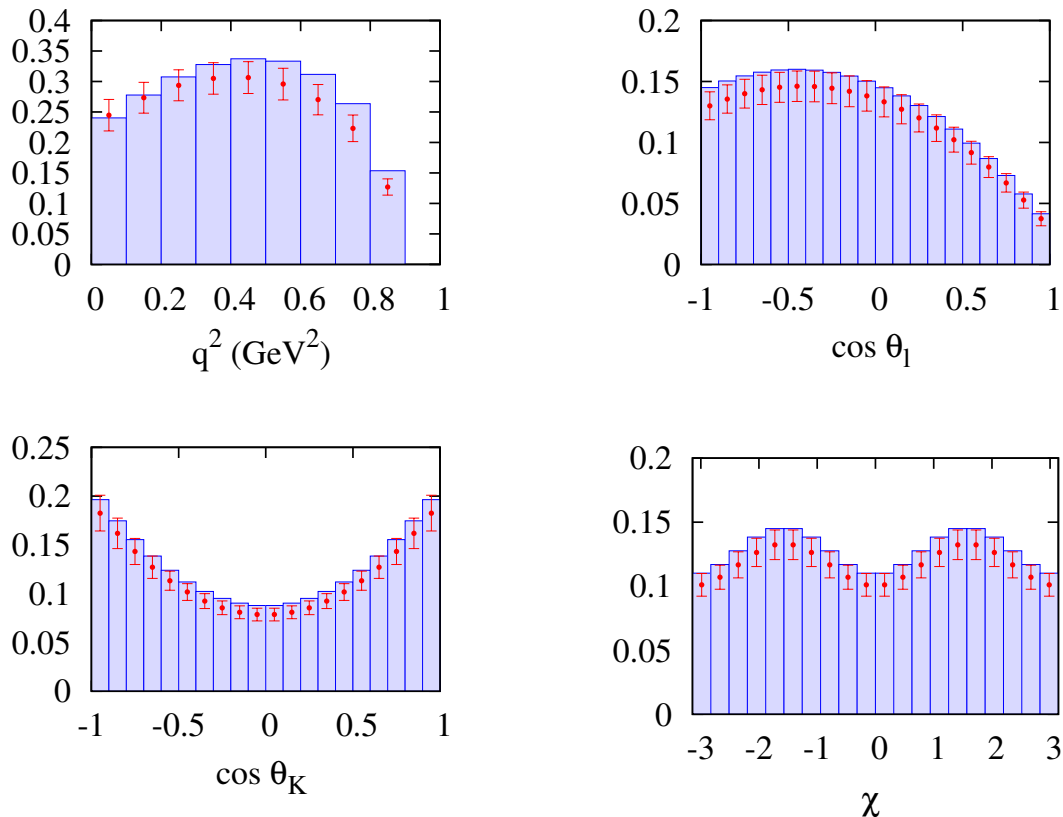


FIG. 7: Decay distributions for  $D_s \rightarrow \phi l \nu$  with  $\phi \rightarrow K^+ K^-$  for each of the kinematic variables in the decay. The decay angles are shown in Figure 1 and described in the text. The lattice results are shown with the red points with error bars and the experimental results by blue blocks. The experimental errors are not plotted, but are of similar size to the lattice errors.

cay and from the  $D \rightarrow K$  form factor and its comparison to  $D$  semileptonic decay. The value from CKM unitarity is also shown. We see that the result from  $D_s \rightarrow \phi$  decay is in good agreement with the other results but has larger errors. This is a combination of both larger lattice QCD and experimental errors. The lattice QCD error is dominated by the statistical error in the determination of the form factors. Although the current calculation did use a large sample of configurations, reducing the statistical error is certainly feasible at these values of the lattice spacing. This would make an improved experimental error, for example from BESIII, highly desirable.

The fact the  $\phi$  has a strong decay to  $K\bar{K}$  and so is not gold-plated is an additional source of uncertainty. Here we have estimated this at 3% based on studies of the  $\phi$  mass and decay constant as well as phenomenological arguments. For the  $\phi$  meson, we find  $M_\phi = 1.032(16)$  GeV and  $f_\phi = 241(18)$  MeV, leading to  $\Gamma(\phi \rightarrow e^+ e^-) = 1.41(21)$  keV, in agreement with experiment (1.27(4) keV [19]). Further studies are underway of the  $\phi$  with improved statistical accuracy and on gluon field configurations that include lighter  $u/d$  quarks going down to physical masses [27]. These should establish to higher accuracy the effect of the strong decay on the  $\phi$  properties.

Several elements of our calculation point the way towards future work. We have been able to determine the pseudoscalar form factor here which contributes to a lepton-mass-suppressed helicity contribution to the decay rate. This could be observed experimentally in the  $D_s \rightarrow \phi \mu \nu$  channel and would give an additional handle to test weak interactions. We have also tested further the fact that heavy meson form factors at a given  $q^2$  value seem to be insensitive to the spectator quark mass (between light and strange masses). Direct tests of this experimentally (for example between  $D_s \rightarrow \phi$  and  $D \rightarrow K^*$ ) would be interesting.

As we have seen here and in other calculations, for example [2, 9], the HISQ action gives very small discretisation errors for  $c$  quarks. This points the way to its use for heavier quark masses. Extrapolations to the  $b$  can be done accurately if results at multiple lattice spacings are available, including very fine lattices [28–30]. The results here demonstrate that we can calculate pseudoscalar to vector meson transitions using HISQ valence quarks with nonperturbative normalisation of the vector and axial vector currents. Working at heavier masses and finer lattices and extrapolating then gives us a new method for determining vector and axial vector form factors for, for example,  $B \rightarrow D^* l \nu$  decays (for determination of  $V_{cb}$ )

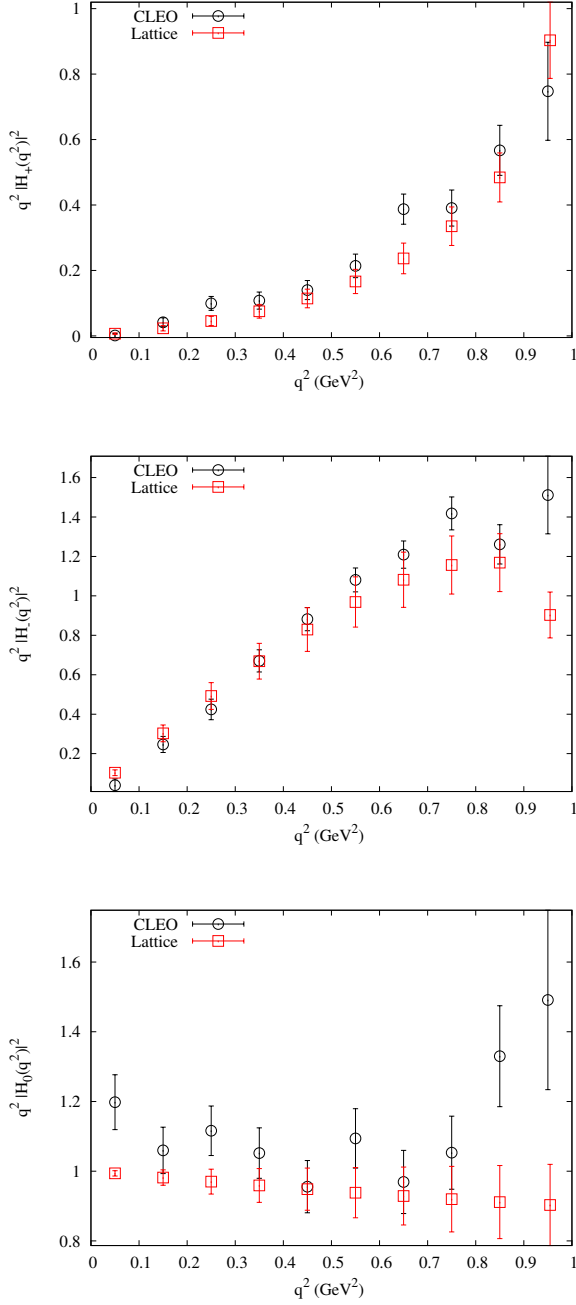


FIG. 8: Comparison of lattice QCD with CLEO’s determination [6] of the helicity amplitudes for  $D \rightarrow K^*$ . We assume that the form factors are insensitive to the spectator quark mass, so we can construct the  $D \rightarrow K^*$  helicity amplitudes using the same form factors as  $D_s \rightarrow \phi$ . The data plotted is normalised such that  $q^2 |H_0(q^2)|^2 \rightarrow 1$  as  $q^2 \rightarrow 0$ .

and  $B_s \rightarrow \phi \ell^+ \ell^-$  decays (to search for new physics).

*Acknowledgements.* We are grateful to MILC for the use of their gauge configurations and to R. Dowdall, E. Follana, S. Playfer and P. Roudeau for useful discussions. We used the Darwin Supercomputer as part of the DiRAC facility jointly funded by STFC, BIS and the

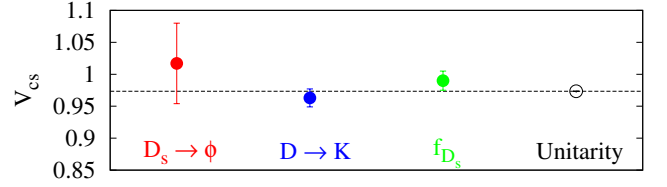


FIG. 9: Comparison of the values of  $V_{cs}$  obtained here from  $D_s \rightarrow \phi$  decay and those from  $D_s$  leptonic decay [8] and  $D \rightarrow K$  semileptonic decay [1]. We also show the result from CKM unitarity [19].

Set	$Z_{\gamma_\mu \otimes 1}^{ss}$	$Z_{\gamma_\mu \otimes \gamma_\mu}^{ss}$	$Z_{\gamma_\mu \otimes \gamma_\mu}^{cs}$	$Z_{\gamma_5 \gamma_\mu \otimes \gamma_5}^{cs}$	$Z_{\gamma_5 \gamma_\mu \otimes \gamma_5 \gamma_\mu}^{cs}$
1	1.104(15)	1.007(12)	1.027(3)	1.065(7)	1.038(3)
2	1.104(15)	1.003(9)	1.020(10)	1.065(5)	1.036(4)
3	1.047(6)	1.009(11)	1.009(2)	1.017(5)	1.020(6)

TABLE V: The  $Z$  factors on each ensemble for the staggered bilinears used. In columns 2 and 3 are the  $Z$  factors for the  $s\bar{s}$  vector currents used for  $f_\phi$ . For  $Z_{\gamma_\mu \otimes 1}$  we use the same result, calculated on set 2, for both coarse lattices, sets 1 and 2, since we do not expect the result to depend significantly on the sea quark masses. In columns 4, 5 and 6, the  $Z$  factors for the local vector, the 1-link axial vector and the local axial vector for the  $c\bar{s}$  weak currents in the  $D_s \rightarrow \phi \ell \nu$  calculations.

Universities of Cambridge and Glasgow. This work was funded by STFC.

### Appendix A: Nonperturbative renormalisation factors for staggered bilinears

For the staggered currents in the correlation functions needed to extract the  $D_s \rightarrow \phi$  form factors and the  $\phi$  decay constant, we have used a number of staggered axial vector and vector operators. We used both a one-link vector with spin-taste  $\gamma_\mu \otimes 1$  and a local vector with spin-taste  $\gamma_\mu \otimes \gamma_\mu$  for the  $\phi$  meson 2-point correlators. The  $D_s \rightarrow \phi$  vector form factor was extracted using a local vector current ( $\gamma_\mu \otimes \gamma_\mu$ ) for the charm to strange transition. The axial vector form factors were extracted using both a one-link point split operator ( $\gamma_5 \gamma_\mu \otimes \gamma_5$ ) and a local axial vector operator ( $\gamma_5 \gamma_\mu \otimes \gamma_5 \gamma_\mu$ ). We have calculated renormalisation factors for each of these operators nonperturbatively. The renormalisation factors,  $Z$ , on each of the ensembles used are given in Table V. The methods used to extract the  $Z$  factors are described in the following sections.

Note that the local scalar ( $1 \otimes 1$ ) and pseudoscalar ( $\gamma_5 \otimes \gamma_5$ ) operators that we use here are absolutely normalised through the partially conserved vector or axial vector current relation. This requires them to be multiplied by, respectively, the difference and sum of the lattice quark masses for the quarks appearing in the current. No  $Z$  factor is then needed for these operators.

### 1. 1-link vector

The matrix element for a general pseudoscalar to pseudoscalar meson transition can be written as

$$\begin{aligned} \langle P(p)|V_\mu|P'(p')\rangle &= f_+(q^2) \left[ p^\mu + p'^\mu - \frac{M_P^2 - M_{P'}^2}{q^2} q^\mu \right] \\ &+ f_0(q^2) \frac{M_P^2 - M_{P'}^2}{q^2} q^\mu, \end{aligned} \quad (\text{A1})$$

where  $P$  and  $P'$  are pseudoscalar mesons with momenta  $p$  and  $p'$  and masses  $M_P$  and  $M_{P'}$  respectively and  $q^\mu = p'^\mu - p^\mu$ .

When  $q^2 = 0$ , the form factors  $f_+(0)$  and  $f_0(0)$  are equal. This can be used to normalise the vector current by making a 3-point function with identical mesons at the source and sink. Eq. A1 reduces to

$$\langle P(p)|V_\mu|P(p)\rangle = 2p^\mu f_+(0). \quad (\text{A2})$$

We normalise the  $V_\mu$  operator by insisting that  $f_+(0) = 1$ , so we have

$$Z \langle P(p)|V_\mu|P(p)\rangle = 2p^\mu. \quad (\text{A3})$$

Here we work with a spatial vector current so this calculation must be done with mesons with the same non-zero momentum.

It is particularly easy to normalise the taste-singlet vector operator ( $\gamma_\mu \otimes 1$ ) in this way because a staggered propagator can be used as the spectator quark in the 3-point correlator. The identical mesons at each end of the 3-point function must be created with operators of the same taste so we get an overall taste-singlet 3-point correlator only if we use the taste-singlet vector operator, which is a 1-link point-split current. To obtain the same non-zero momentum for the source and sink mesons we calculate the spectator quark propagator with a phased boundary condition as in Eq. 9 [17]. The 3-point correlator for an  $\eta_s \rightarrow \eta_s$  3-point function with this vector current inserted between strange propagators is then

$$\begin{aligned} C_{3pt}(0, t, T) &= \sum_{x,y,z} (-1)^{y_\mu} \varepsilon(y) \varepsilon(z) \\ &\times \text{Tr} [g_s^\theta(x, z) g_s(z, y) g_s^\dagger(x, y \pm \hat{\mu})]. \end{aligned} \quad (\text{A4})$$

As before, the sites  $x$ ,  $y$  and  $z$  are at times 0,  $t$  and  $T$  respectively and we sum over lattice sites on the same timeslice.

To obtain the  $Z$  factors the 3-point correlators are fitted, along with the appropriate 2-point correlators, according to the fit form given in Eq. 11. For the  $\eta_s$  we use the Goldstone pseudoscalar operator so that the 2-point correlator is simply the modulus squared of the strange quark propagator. Since the 3-point function is symmetric in this case, with identical mesons at 0 and  $T$ , we can impose on the fit that  $V^{nn}$  and  $V^{oo}$  are symmetric matrices and  $V^{on} = V^{no}$ .

Set	$am_h$	$T$ values	$Z$
1	2.0	15,16,20,21	1.007(12)
2	2.0	15,16,20,21	1.003(9)
		2.8	15,16,20,21
3	1.5	24,25,30,31	1.009(11)

TABLE VI: Further details for the calculation of the  $Z$  factors on each ensemble for the local  $\bar{s}(\gamma_\mu \otimes \gamma_\mu)s$  operator. 4 time sources were used per configuration. The NRQCD masses used are given in column 2. For ensemble 2, two masses were used for the NRQCD spectator quark. Column 3 gives the values of  $T$  used for the 3-point correlators and column 4 gives the  $Z$  factor.

The  $Z$  factors obtained for the 1-link taste-singlet vector current are given in Table V [31] and are labelled as  $Z_{\gamma_\mu \otimes 1}^{s\bar{s}}$ . Note that the  $Z$  factors in this case are significantly different from 1. The  $Z$  factor was shown in [31] to be independent of the spatial momentum used for the spectator quark and of whether the spectator was a charm or strange quark (i.e. comparing  $\eta_s \rightarrow \eta_s$  with  $D_s \rightarrow D_s$ ). We also found that the  $Z$  factor did not change significantly between a  $c\bar{c}$  and  $s\bar{s}$  current.

### 2. Local vector

We use a local vector current for  $f_\phi$  with equal mass (both strange) quarks. We also use the same operator with unequal quark masses for the charm to strange transition in  $D_s \rightarrow \phi$ . The  $Z$  factors for these two cases are calculated with different methods. In both cases, it is simplest to normalise the temporal vector; for the relativistic HISQ action the renormalisation factors for the spatial and temporal components will differ only by discretisation effects which vanish in the continuum limit. For a temporal vector current renormalisation we can work with mesons at rest.

#### a. Equal quark mass case

As the local vector operator is not a taste-singlet, it cannot simply be inserted into a pseudoscalar to pseudoscalar symmetric 3-point function where staggered quarks are used for each of the propagators. However, it can be normalised using a 3-point function where the spectator quark retains 4 spin components. Here it is convenient to use NRQCD for the spectator quark, as we did for the local charm-charm vector operator in [9]. The staggered-staggered current renormalisation factor should not depend (up to discretisation effects) on the details of the spectator quark, so there is no need for the NRQCD quark mass to correspond to a physical quark.

To combine a staggered propagator with one carrying spin indices, we convert the staggered propagator to a 4-spin naive propagator using the products of  $\gamma$  matrices

ces (here denoted  $\Omega$ ) which diagonalise the naive quark action in spin space [2]. A staggered-NRQCD 2-point correlator is given by

$$C_{2pt}(0, t) = \sum_{x, y} \text{Tr} \{ G_{\text{NRQCD}}(x, y) \Omega(y) g^\dagger(x, y) \Omega^\dagger(x) \}, \quad (\text{A5})$$

where sites  $x$  and  $y$  are at times 0 and  $t$ , the sum is over timeslices and the trace is over both spin and colour. The staggered propagator  $g(x, y)$  contains no spin dependence and the  $\Omega$  matrices contain no colour, so that the traces in the correlator can be separated:

$$C_{2pt}(0, t) = \sum_{x, y} \text{Tr}_c \{ \text{Tr}_s [\Omega^\dagger(x) G_{\text{NRQCD}}(x, y) \Omega(y)] g^\dagger(x, y) \}. \quad (\text{A6})$$

This shows that we can take the spin trace after multiplying the NRQCD propagator by the  $\Omega$  matrices and we can do this before combining it with the staggered propagator.

We can extend this to 3-point functions and take the spin trace of the NRQCD propagator and  $\gamma$  matrices in the middle of the calculation. The 3-point correlation function is

$$C_{3pt}(0, t, T) = \sum_{x, y, z} \varepsilon(z) (-1)^{y_t} \times \text{Tr}_c \{ \text{Tr}_s [\gamma_t \Omega^\dagger(x) G_{\text{NRQCD}}(x, z) \Omega(z)] g(z, y) g^\dagger(x, y) \}, \quad (\text{A7})$$

where sites  $x$ ,  $y$  and  $z$  are at times 0,  $t$  and  $T$ . The NRQCD propagator is the spectator (propagator 1 in Fig. 2). We use  $\sum_x \varepsilon(z) \text{Tr}_s [\gamma_t \Omega^\dagger(x) G_{\text{NRQCD}}(x, z) \Omega(z)]$  as the source for the inversion of extended propagator 2.

We calculate the NRQCD-HISQ 2-point and 3-point functions for different  $T$  values. Details of the parameters used and results are given in Table VI. Up to discretisation effects,  $Z$  should not depend on the mass of the spectator quark. On ensemble 2, the  $Z$  factor was calculated using two values of the heavy NRQCD quark mass,  $am_h$ , and the results agree within the statistical errors. The  $Z$  factors used to normalise the current for  $f_\phi$  are the ones obtained with  $am_h = 2.0$  for the coarse ensembles 1 and 2 and  $am_h = 1.5$  for the fine ensemble 3. These NRQCD masses correspond to approximately the same physical quark mass.

We summarise our results for  $Z_{\gamma_\mu \otimes \gamma_\mu}^{c\bar{s}}$  in Table V. Values are close to 1 for this vector operator.

### b. Unequal quark mass case

The local temporal  $c\bar{s}$  vector can be normalised using a local non-Goldstone  $D_s$  (made with a  $\gamma_t \gamma_5 \otimes \gamma_t \gamma_5$  operator) in a  $D_s \rightarrow \eta_s$  3-point correlator with both the  $D_s$  and  $\eta_s$  at rest. From Eq. A1 we see that the matrix element is then given by  $f_0(q_{max}^2)(M_P + M_{P'})$ , up

to a  $Z$  factor for the vector current. By comparing this to the result from the absolutely normalised local scalar current between the Goldstone  $D_s$  and  $\eta_s$  we can extract  $Z$  [1, 25]. The scalar current matrix element is given by:

$$\langle P(p) | S | P'(p') \rangle = f_0(q^2) \frac{M_{P'}^2 - M_P^2}{m_{01} - m_{02}} \quad (\text{A8})$$

where  $P'$  is a  $D_s$  meson,  $P$ , an  $\eta_s$ ,  $m_{01}$  is the lattice charm quark mass and  $m_{02}$ , the lattice strange quark mass.

The difference in mass between the Goldstone and non-Goldstone  $D_s$  is a small lattice artefact which will mean that  $q_{max}^2$  is not quite the same in the two cases. These two masses appear in Table III; we use a Goldstone  $D_s$  in our extraction of the axial vector form factors and the non-Goldstone  $D_s$  is used when calculating the vector form factor. We see that the difference between them is very small even on the coarse lattices, and is clearly vanishing rapidly as the lattice spacing goes to zero.

The renormalisation factors that we obtain from this method are given in Table V as  $Z_{\gamma_\mu \otimes \gamma_\mu}^{c\bar{s}}$ . Similarly to the equal mass case, they have values close to 1.

### 3. 1-link axial vector

The 1-link axial vector operator ( $\gamma_\mu \gamma_5 \otimes \gamma_5$ ) that we use includes a point-splitting in the same spatial direction as the polarization of the axial vector. It therefore has the same taste as local pseudoscalar operator and the partially conserved axial current, and we can use this to normalise it. For the HISQ action, the partially conserved axial current relation gives

$$p_\mu \langle 0 | A_\mu | P_0 \rangle = (m_{01} + m_{02}) \langle 0 | \gamma_5 | P_0 \rangle \quad (\text{A9})$$

for a pseudoscalar meson  $P_0$  with valence quarks of lattice quark masses  $m_{01}$  and  $m_{02}$ .

We can then normalise the 1-link axial vector operator using a correlation function where  $P_0$  is created using a local pseudoscalar and destroyed with a 1-link axial vector. The correlator is

$$C_{PS \rightarrow AV}(0, t) = i \sum_{x, y} (-1)^{y_\mu} \times \text{Tr} \left[ g_1(x, y) g_2^\dagger(x, y \pm \hat{\mu}) \right] \quad (\text{A10})$$

where  $x$  is at time 0 and  $y$  at  $t$ . The point-splitting at  $y$  is implemented by averaging over links in the forward and backward directions. We fit simultaneously with the pseudoscalar 2-point correlator where  $P_0$  is created and destroyed by the same local pseudoscalar operator, given by

$$C_{PS \rightarrow PS}(0, t) = \sum_{x, y} \text{Tr} \left[ g_1(x, y) g_2^\dagger(x, y) \right]. \quad (\text{A11})$$

The form of the fit used is given for the 2-point function in Eq. 11. Since we have different operators at the source and sink for the  $C_{PS \rightarrow AV}$  correlators, the amplitudes for

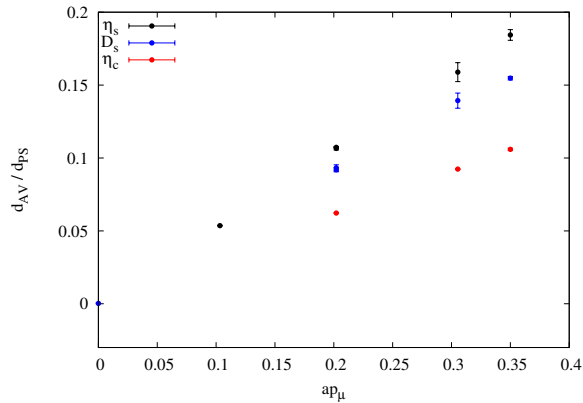


FIG. 10: The ratio of axial vector and pseudoscalar amplitudes plotted against meson momentum in lattice units for pseudoscalar mesons made from  $c$  and  $s$  valence quarks. The results come from coarse lattices, set 2. This ratio is proportional to the momentum and the renormalisation factor for the axial vector operator can be extracted from the gradient of the line, given by  $\frac{m_{01} + m_{02}}{M_{P_0}^2} \frac{1}{Z}$ .

each state in that case are the product of a source operator amplitude and a sink operator amplitude. Thus, for the ground-state, the amplitude in  $C_{PS \rightarrow PS}$  is  $d_{PS}^2$  and for  $C_{PS \rightarrow AV}$  it is  $d_{PS}d_{AV}$ .

Including the  $Z$  factor for the operator, the axial vector fit amplitude  $d_{AV}$  is then related to the pseudoscalar amplitude  $d_{PS}$  through Eq. A9 by

$$Zd_{AV} = \frac{m_{01} + m_{02}}{M_{P_0}^2} p_\mu d_{PS}. \quad (\text{A12})$$

Because the  $\mu$  direction is spatial here, we need to include momentum in the meson to normalise the axial vector operator in this way.

The ratio  $d_{AV}/d_{PS}$  is plotted against the meson momentum for pseudoscalar mesons containing charm and strange quarks for coarse set 2 in Figure 10. From Eq. A12, the ratio should be proportional to  $p_\mu$ , where the  $\mu$  is the direction of the axial vector, and we see that the results indeed do give straight lines through the origin. The  $Z$  factor can then be extracted from the gradient, which is  $(m_{01} + m_{02})/(M_{P_0}^2 Z)$ .

If the quark masses are unequal and we use the 1-link operator in Eq. A10, then we find a dependence on which quark propagator carries the meson's momentum. For the  $c\bar{s}$  current that we use, the operator is normalised with the  $s$  quark carrying the momentum. This is the same situation as appears in the  $D_s \rightarrow \phi$  3-point functions. The effects of including momentum in point-split operators are discussed further in Appendix B. We find that the dependence on which quark carries the momentum is a lattice spacing artefact.

The values we obtain for  $Z_{\gamma_5 \gamma_\mu \otimes \gamma_5}^{c\bar{s}}$  for each ensemble are given in Table V.

#### 4. Local axial vector

The temporal component of the local axial vector ( $\gamma_5 \gamma_t \otimes \gamma_5 \gamma_t$ ) can be normalised by comparing amplitudes for Goldstone and local non-Goldstone pseudoscalar meson correlators. To normalise the  $c\bar{s}$  current which appears in the charm to strange decay, we simply demand that the matrix element for the temporal axial current be the same for Goldstone and non-Goldstone  $D_s$  mesons.

From fits to the separate Goldstone and non-Goldstone correlators we obtain amplitudes for the ground-state of  $d_{PS}$  and  $d_{LTA V}$  respectively. And then, from Eq. A12 but for the temporal case at zero momentum, we have normalisation condition

$$Zd_{LTA V} = \frac{(m_{0c} + m_{0s})}{M_{D_s}} d_{PS}. \quad (\text{A13})$$

As before, a small discretisation effect arises from the fact that the masses of the Goldstone and non-Goldstone  $D_s$  are not exactly the same at non-zero lattice spacing. The renormalisation factor,  $Z_{\gamma_5 \gamma_\mu \otimes \gamma_5 \gamma_\mu}^{c\bar{s}}$ , is easily extracted and given in Table V.

#### Appendix B: Point-split operators with momentum

Here we consider an issue with momentum and point split operators, which arises for the pseudoscalar to axial vector correlators we consider in Appendix A 3. For quark propagators carrying momentum, we use boundary conditions that incorporate a phase as in Eq. 9 [16, 17]. A propagator  $g_1^{\theta_a}(x, y)$  for a quark with mass  $m_1$  carrying momentum  $p^a$  is related to propagator calculated without twisted boundary conditions by

$$g_1^{\theta_a}(x, y) = g_1(x, y) e^{-i\theta_a(x-y)} \quad (\text{B1})$$

where  $p_a = \theta_a/L_s$  for a lattice of spatial size  $L_s$ .

For the 1-link spatial axial vector current, we implement a symmetric point-splitting at the sink in, say, the  $\mu$  direction and write the correlator as

$$\frac{i}{2} g_1^{\theta_1 \dagger}(x, y) \left\{ g_2^{\theta_2}(x, y + \hat{\mu}) + g_2^{\theta_2}(x, y - \hat{\mu}) \right\} \quad (\text{B2})$$

omitting the sum over timeslices, staggered phase and colour trace. Note that the staggered phase in Eq. A10 does not contain  $(-1)^{y_\mu}$  which means that the phase factor is the same at  $y$  and  $y \pm \hat{\mu}$ .

The meson made of quarks 1 and 2 has total momentum  $\theta_{total} = \theta_2 - \theta_1$  so the twisted boundary condition only needs to be applied in one of the inversions. Also different combinations of  $\theta_1$  and  $\theta_2$  should give the same result for the same  $\theta_{total}$ . When the two quarks have equal mass it makes no difference, but in the unequal mass case the simple operator in Eq. B2 shows results that depend on which quark carries which momentum.

The simplest case to study is that in which the total momentum given by  $\theta$  is zero. Then the amplitude of

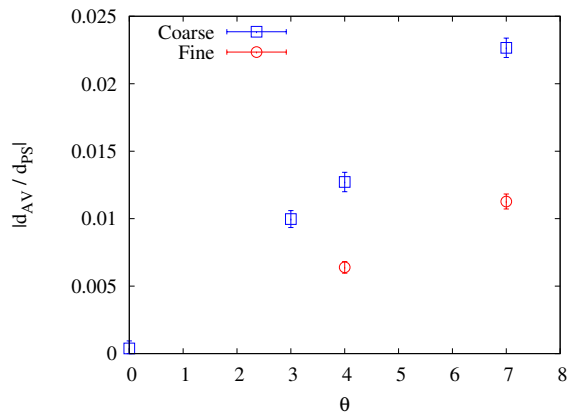


FIG. 11: The ratio of the axial vector to pseudoscalar amplitudes in the case where the charm and strange propagators carry the same phase at the boundary,  $\theta$ . In this case, the total meson momentum is zero and we expect this ratio to be zero. The ratio is plotted against the momentum carried (in opposite directions) by each propagator. The blue squares are for the coarse Set 2 and the red circles for fine Set 3. These gauge configurations have approximately the same physical size, so the same  $\theta$  corresponds to the same physical momentum on each.

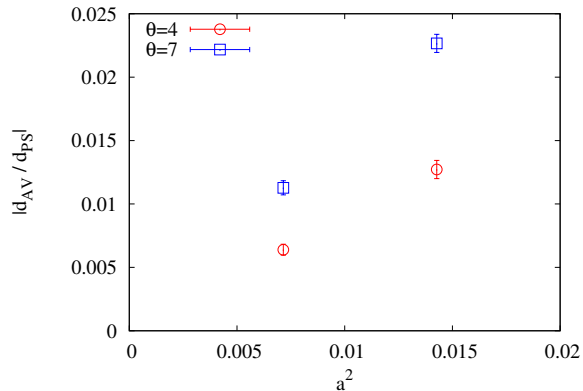


FIG. 12: The ratio of the axial vector to pseudoscalar amplitudes in the case where the charm and strange propagators carry the same twist. In this case, the total meson momentum is zero and we expect this ratio to be zero. The ratio is plotted against  $a^2$ . Sets 2 and 3 have different lattice spacing, but the same physical size so the same twist  $\theta$  on each corresponds to the same physical momentum. The red and blue data points are for the cases in which both the strange and charm propagators carry  $\theta = 4, 7$ .

the spatial axial vector current between the vacuum and a pseudoscalar meson (i.e.  $d_{AV}$  in Appendix A 3) should be zero. Putting momentum  $\theta_2 = \theta_1 = \theta$  and writing Equation B2 in terms of propagators with no twist gives

$$\frac{i}{2} g_1^\dagger(x, y) \{ g_2(x, y + \hat{\mu}) e^{i\theta} + g_2(x, y - \hat{\mu}) e^{-i\theta} \}. \quad (\text{B3})$$

This should give zero for all values of  $\theta$  when summed over  $y$ . In the equal mass case this is true because the

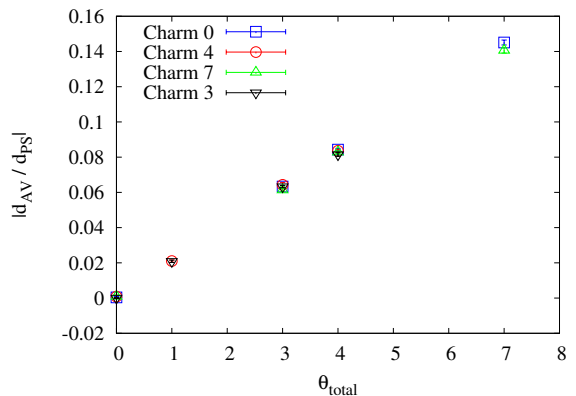


FIG. 13: The ratio of axial vector to pseudoscalar fit amplitudes plotted against  $D_s$  total momentum (given by the difference of phases carried by the  $c$  and  $s$  quarks), where the 1-link axial vector operator is given by Eq. B4. The different symbols indicate the momentum (phase at the boundary) carried by the charm quark. Results are for the coarse lattices, set 2. Now the amplitude ratio agrees for points where the meson total momentum is same.

two pieces are complex conjugates of each other so the real part of the correlator is zero (configuration by configuration).

In the unequal mass case the amplitude is not zero and depends on  $\theta$ . In Figure 11, we plot the ratio for  $D_s$  mesons created this way on both fine and coarse gauge configurations. The data is from Sets 2 and 3 with approximately the same lattice length in physical units ( $aL_s$ ) so the same  $\theta$  on each corresponds to the same physical momentum. We see that the difference of the ratio from zero depends linearly on the momentum carried by each quark, denoted by  $\theta$ . We also see, however, that the difference is less on the fine lattices than on the coarse. A similar situation holds for non-zero meson momentum in that the amplitude ratio shows a spread which depends on how that momentum is made up from the quark momenta.

In Figure 12, we plot the same zero momentum meson data as in Figure 11, but now against  $a^2$ . For each value of  $\theta$ , we see that the discrepancy depends on  $a^2$ . This demonstrates that the ambiguity in which quark carries the meson's momentum is a discretisation error. In our results (as discussed in Appendix A 3) we have determined  $Z$  using twisted boundary conditions for the  $s$  quark. The results above show that the same results would be obtained in the continuum limit if instead we had used twisted boundary conditions for the  $c$  quarks.

The difference can be avoided by using a definition of the point-split operator that is less affected by the way in which the momentum is split between the propagators, and is more symmetric. One example would be to combine propagators  $g_1^{\theta_1}(x, y)$  carrying momentum  $\theta_1$  and

$g_2^{\theta_2}(x, y)$  carrying  $\theta_2$  in the following way:

$$\frac{i}{4} \left\{ g_1^{\theta_1 \dagger}(x, y) g_2^{\theta_2}(x, y + \hat{\mu}) e^{-i\theta_2} + g_1^{\theta_1 \dagger}(x, y + \hat{\mu}) g_2^{\theta_2}(x, y) e^{i\theta_1} + g_1^{\theta_1 \dagger}(x, y) g_2^{\theta_2}(x, y - \hat{\mu}) e^{i\theta_2} + g_1^{\theta_1 \dagger}(x, y - \hat{\mu}) g_2^{\theta_2}(x, y) e^{-i\theta_1} \right\} \quad (\text{B4})$$

which has meson momentum  $\theta_{total} = \theta_2 - \theta_1$ . If the meson is to carry momentum  $\theta$  using only a phase in the quark propagator  $g_2(x, y)$ , then we have  $\theta_1 = 0, \theta_2 = \theta$  and if the momentum is carried only by  $g_1(x, y)$  then  $\theta_1 = -\theta, \theta_2 = 0$ . In either case, writing Eq. B4 in terms of propagators calculated without twisted boundary con-

ditions gives

$$\frac{i e^{-i\theta(x-y)}}{4} \left\{ g_1^{\dagger}(x, y) g_2(x, y + \hat{\mu}) + g_1^{\dagger}(x, y + \hat{\mu}) g_2(x, y) + g_1^{\dagger}(x, y) g_2(x, y - \hat{\mu}) + g_1^{\dagger}(x, y - \hat{\mu}) g_2(x, y) \right\}. \quad (\text{B5})$$

This is also true for all  $\theta_1$  and  $\theta_2$  that satisfy  $\theta_2 - \theta_1 = \theta$ .

Using this form of the 1-link axial vector operator gives the axial vector to pseudoscalar amplitude ratios for the  $D_s$  shown in Figure 13. Now we see that the amplitude is zero at zero meson momentum and we have good agreement between amplitude ratios for a given meson momentum that correspond to a different distribution of momentum between  $s$  and  $c$  quarks.

- 
- [1] J. Koponen, C. Davies, G. Donald, E. Follana, G. Lepage, et al. (HPQCD Collaboration) (2013), 1305.1462.
- [2] E. Follana et al. (HPQCD and UKQCD Collaborations), Phys.Rev. **D75**, 054502 (2007), hep-lat/0610092.
- [3] J. D. Richman and P. R. Burchat, Rev.Mod.Phys. **67**, 893 (1995), hep-ph/9508250.
- [4] B. Aubert et al. (BaBar Collaboration), Phys.Rev. **D78**, 051101 (2008), 0807.1599.
- [5] J. Korner and G. Schuler, Z.Phys. **C46**, 93 (1990).
- [6] R. Briere et al. (CLEO Collaboration), Phys.Rev. **D81**, 112001 (2010), 1004.1954.
- [7] E. Follana, C. Davies, G. Lepage, and J. Shigemitsu (HPQCD and UKQCD Collaborations), Phys.Rev.Lett. **100**, 062002 (2008), 0706.1726.
- [8] C. Davies, C. McNeile, E. Follana, G. Lepage, H. Na, et al. (HPQCD Collaboration), Phys.Rev. **D82**, 114504 (2010), 1008.4018.
- [9] G. Donald, C. Davies, R. Dowdall, E. Follana, K. Hornbostel, et al. (HPQCD Collaboration), Phys.Rev. **D86**, 094501 (2012), 1208.2855.
- [10] A. Bazavov, D. Toussaint, C. Bernard, J. Laiho, C. Detar, et al., Rev.Mod.Phys. **82**, 1349 (2010), 0903.3598.
- [11] C. Davies, E. Follana, I. Kendall, G. Lepage, and C. McNeile (HPQCD Collaboration), Phys.Rev. **D81**, 034506 (2010), 0910.1229.
- [12] E. B. Gregory et al. (HPQCD collaboration), Phys. Rev. **D83**, 014506 (2011), 1010.3848.
- [13] S. Naik, Nucl.Phys. **B316**, 238 (1989).
- [14] A. Bazavov et al. (MILC Collaboration) (2012), 1212.4768.
- [15] C. McNeile, C. Michael, and K. Sharkey (UKQCD Collaboration), Phys.Rev. **D65**, 014508 (2002), hep-lat/0107003.
- [16] G. de Divitiis, R. Petronzio, and N. Tantalo, Phys.Lett. **B595**, 408 (2004), hep-lat/0405002.
- [17] D. Guadagnoli, F. Mescia, and S. Simula, Phys.Rev. **D73**, 114504 (2006), hep-lat/0512020.
- [18] G. P. Lepage et al., Nucl. Phys. Proc. Suppl. **106**, 12 (2002), hep-lat/0110175.
- [19] J. Beringer et al., Phys. Rev. D **86**, 010001 (2012).
- [20] J. J. Dudek, R. G. Edwards, B. Joo, M. J. Peardon, D. G. Richards, et al., Phys.Rev. **D83**, 111502 (2011), 1102.4299.
- [21] F. Close, *An Introduction to Quarks and Partons* (Academic Press, 1979).
- [22] M. C. Arnesen, B. Grinstein, I. Z. Rothstein, and I. W. Stewart, Phys.Rev.Lett. **95**, 071802 (2005), hep-ph/0504209.
- [23] R. J. Hill, eConf **C070805**, 22 (2007), 0712.3817.
- [24] C. Bourrely, I. Caprini, and L. Lellouch, Phys.Rev. **D79**, 013008 (2009), 0807.2722.
- [25] H. Na, C. T. Davies, E. Follana, G. P. Lepage, and J. Shigemitsu (HPQCD Collaboration), Phys.Rev. **D82**, 114506 (2010), 1008.4562.
- [26] J. Link et al. (FOCUS Collaboration), Phys.Lett. **B586**, 183 (2004), hep-ex/0401001.
- [27] B. Chakraborty et al. (HPQCD Collaboration), PoS **LATTICE2013** (2013).
- [28] C. McNeile, C. Davies, E. Follana, K. Hornbostel, and G. Lepage (HPQCD Collaboration), Phys.Rev. **D82**, 034512 (2010), 1004.4285.
- [29] C. McNeile, C. Davies, E. Follana, K. Hornbostel, and G. Lepage (HPQCD Collaboration), Phys.Rev. **D85**, 031503 (2012), 1110.4510.
- [30] C. McNeile, C. Davies, E. Follana, K. Hornbostel, and G. Lepage (HPQCD Collaboration), Phys.Rev. **D86**, 074503 (2012), 1207.0994.
- [31] J. Koponen et al. (HPQCD Collaboration), PoS **LATTICE2011**, 286 (2011), 1111.0225.